Supporting Information

Controlling the fractal dimension in self-assembly of terpyridine modified insulin by Fe^{2+} and Eu^{3+} to direct *in vivo* effect

N. K. Mishra,[a] M. Østergaard[b], S. R. Midtgaard[c], S. S. Strindberg[d], S. Winkler,[b] S. Wu[b], T. J. Sørensen[b], T. Hassenkam[b], J.-C. N. Poulsen[b], L. Lo Leggio[b], H. M. Nielsen[d], L Arleth[c], N. J. Christensen*[a], P. W. Thulstrup*[b], and K. J. Jensen*[a]

[a] Center for Biopharmaceuticals and Biobarriers in Drug Delivery and Department of Chemistry, University of Copenhagen, Thorvaldsensvej 40, DK-1871 Frederiksberg C, Denmark
[b] Department of Chemistry, University of Copenhagen, Universitetsparken 5, DK-2100 Copenhagen Ø, Denmark
[c] The Niels Bohr Institute, University of Copenhagen Universitetsparken 5, DK-2100 Copenhagen Ø, Denmark
[d] Center for Biopharmaceuticals and Biobarriers in Drug Delivery and Department of Pharmacy, University of Copenhagen, Universitetsparken 2, DK-2100 Copenhagen Ø, Denmark

1.0 Experimental methods:

1.1 Material:

2,2':6',2"-Terpyridine-4'-carboxylic acid was purchased from *A*lfa *A*esar. Recombinant Human insulin was purchased from Thermo Fischer USA. All other chemicals were purchased from Sigma-Aldrich (Denmark) and used as received without further purification. MilliQ H_2O was used for aqueous preparations. High-resolution mass spectrometry was obtained on an UHPLC-MS with a QTOF Impact HD (Bruker) and Dionex UltiMate 3000 (Thermo) system equipped with a Kinetex® 2.6 µm EVO C18 100 Å column (50 × 2.1 mm, Phenomenex). Purification of conjugates was performed on Biotage® Isolera™ (HPFC) using C18 column (SNAP Ultra, C18, 300 Å). An aqueous acetonitrile solution (including 0.1% formic acid) was used as the mobile phase with gradient elution for purification.

1.2 Synthesis:

Synthesis of 2,2':6',2"-terpyridine-4'-carboxylic acid NHS ester: 2,2':6',2"-terpyridine-4'-carboxylic acid (100 mg), and TSTU (13.0 mg) were dissolved in DMF (1 mL). DIPEA was added and the solution was stirred overnight. The product was precipitated by addition of H_2O (40 mL) and centrifuged for 30 min. The supernatant was decanted, and the pellet was suspended in H_2O (10 mL) and lyophilized to give the product as a light brown powder. (92 mg, 68.1 %)
^{1}H NMR (300 MHz, $CDCl_3$): 9.07 (s, 2H), 8.71 (m, 2H), 8.59 (m, 2H), 7.87 (td, 2H), 7.37 (m, 2H), 2.94 (bs, 4H).
^{13}C NMR (126 MHz, DMSO): 170.56, 161.52, 157.23, 153.92, 150.12, 138.29, 134.99, 125.79, 121.54, 119.73, 40.52, 40.43, 25.68.

1.21 Synthesis of Lys^{B29}2,2':6',2"-terpyridine-4'-carbamide Human Insulin (Lys^{B29}Tpy-HI):

Human insulin (100 mg, 0.0172 mmol) was suspended in 0.1 M tris Buffer (1.0 mL), the pH was adjusted to 10.5 to dissolve it completely, 2,2':6',2"-terpyridine-4'-carboxylic acid NHS ester (13.0 mg, 0.0361 mmol, 2.1 equivalent) was dissolved in DMF (2.0 mL), added dropwise over 5 minutes to the stirring solution of Human insulin, and allowed the reaction mixture to stir for 15.0 min. The reaction was monitored by LCMS.[1-3] Then reaction mixture was diluted with 10.0 mL of H_2O and pH was adjusted to pH 7.8. Product was isolated using Isolera, applying Biotage SNAP ultra-column (C18, 60 g, 25 um). CH_3CN/H_2O mixed with 0.1% formic

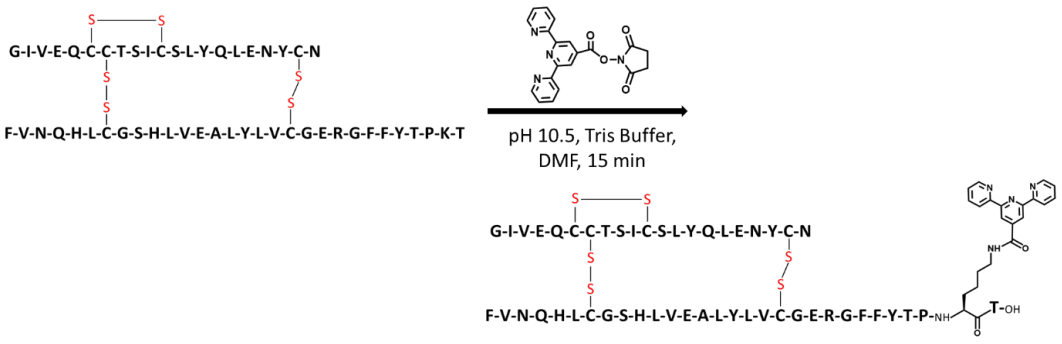

Scheme S1: Synthetic scheme for Lys^{B29}*Tpy*-HI

acid was used as eluents at a linear gradient of 5-50 % CH_3CN over 20 minutes, and a flow rate of 50 mL/min. Each fraction was analyzed. Monosubstituted and disubstituted products were collected separately, CH_3CN was removed at reduced pressure using rotatory evaporator, followed by lyophilized to give product as a white powder (Lys^{B29}*Tpy*-HI-Yield: 32.0 mg, 31 %). (Gly^{A1}-*Tpy*-Lys^{B29}*Tpy*-HI-Yield: 12.0 mg, 11 %). [1-3]

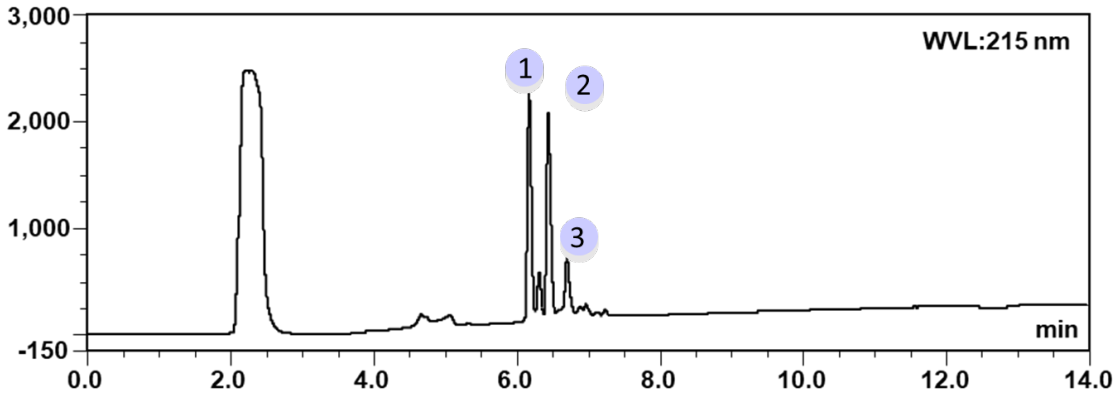

Figure S1: LCMS chromatogram for the crude mixture from the reaction of human insulin with terpyridine-4'-carboxylic NHS ester. **Peak 1** corresponds to unreacted human insulin, **peak 2** corresponds to monosubstituted insulin, **peak 3** corresponds to disubstituted insulin.

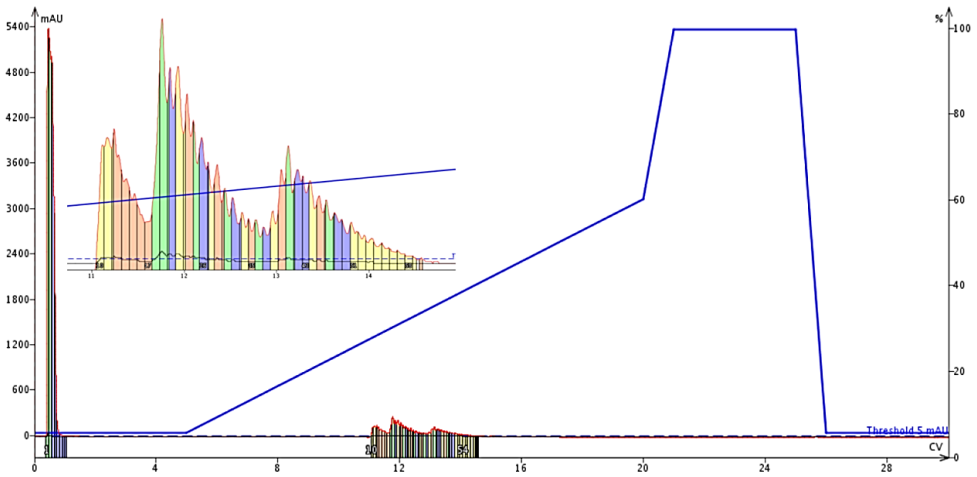

Figure S2: HPFC chromatogram for the purification of Lys^{B29}*Tpy*-HI. Inset shows the zoomed view of collected fraction. Each sample was analyzed through LCMS to achieve the maximum purity of desired product.

LCMS Details: Molecular Formula of Lys^{B29}*Tpy*-HI: $C_{273}H_{392}N_{68}O_{78}S_6$**: Calculated:** 6062.712. **Calculated**: $[M+3H]^{3+}$: 2022.915, $[M+4H]^{4+}$: 1517.438, $[M+5H]^{5+}$: 1214.152, $[M+6H]^{6+}$: 1011.961.
Observed: $[M+3H]^{3+}$: NO, $[M+4H]^{4+}$: 1517.0, $[M+5H]^{5+}$: 1213.7, $[M+6H]^{6+}$: 1011.6.

Table S1: LCMS analysis of Lys^{B29}*Tpy*-HI			
Serial No.	**Peak**	**Calculated**	**Observed**
1.	$[M]^+$	6064.7189	Not Observed
2.	$[M+H]^+$	6065.726	Not observed
3.	$[M+2H]^{2+}$	3033.3667	Not observed
4.	$[M+3H]^{3+}$	2022.91	Not Observed
5.	$[M+4H]^{4+}$	1517.438	1517.0
6.	$[M+5H]^{5+}$	1214.152	1213.7
7.	$[M+6H]^{6+}$	1011.961	1011.6

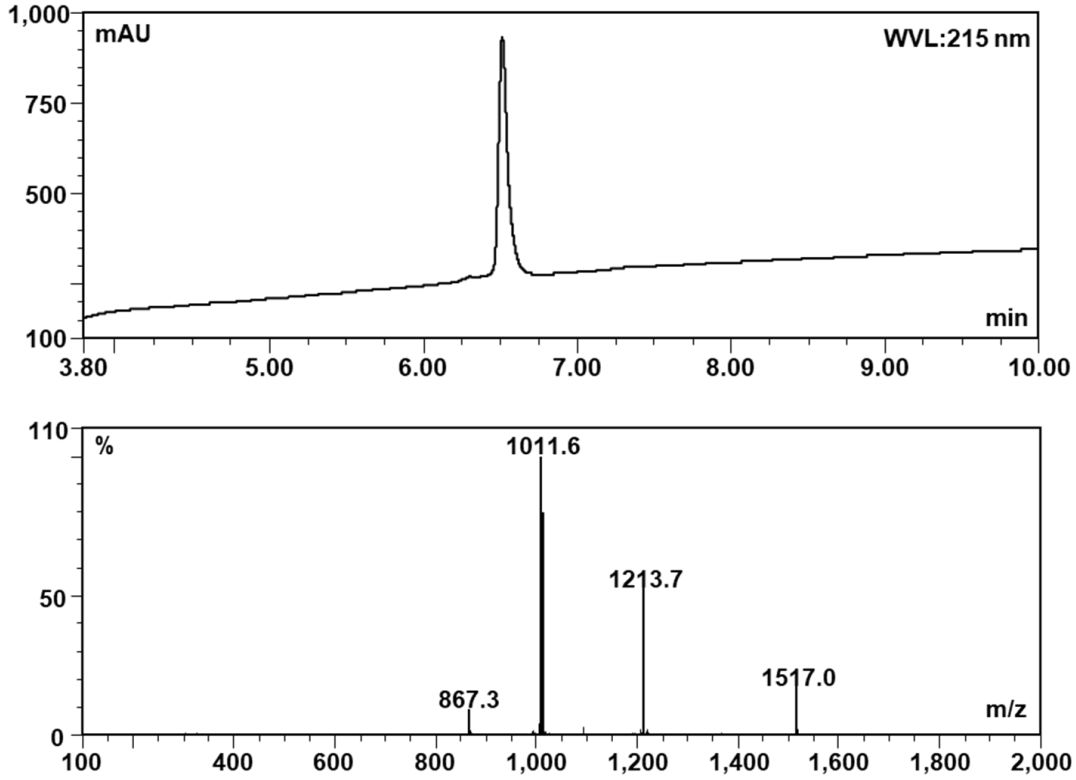

Figure S3: LCMS chromatogram and mass spectrum of Lys^{B29}*Tpy*-HI after purification.

V8 Enzymatic analysis of Lys^{B29}*Tpy*-HI:

The substitution pattern in Lys^{B29}*Tpy*-HI was confirmed by enzymatic digest by treatment with end proteinase Glu-C from Staphylococcus. The fragment analysis confirmed that terpyridine was attached at Lys^{B29} in human insulin.

- **Gly^{A1}-Glu^{A4}** ($C_{18}H_{32}N_4O_7$) **Calculated**: 416.22, **Observed**: Not Observed.
- **Gln^{A5}-Glu^{A17} + Phe^{B1}-Glu^{B13}** ($C_{126}H_{194}N_{34}O_{41}S_4$) Calculated $[M+2H]^{2+}$: 1485.160, **Observed:** 1485.636.
- **Asn^{A18}-Asn^{A21} + Ala^{B14}- Glu^{B21}** ($C_{59}H_{88}N_{14}O_{20}S_2$) Calculated $[M+H]^+$: 1378.589, **Observed**: 1378.556.
- **Arg^{B22}-Lys^{B29}*Tpy*-Thr^{B30}** ($C_{70}H_{86}N_{14}O_{20}S_2$) Calculated: $[M+H]^+$: 1376.665, **Observed**: $[M+H]^+$: 1376.625.

1.3 Synthesis of Phe^{B1}-2,2':6',2"-terpyridine-4'-carbamide Human Insulin (Phe^{B1}Tpy-HI):

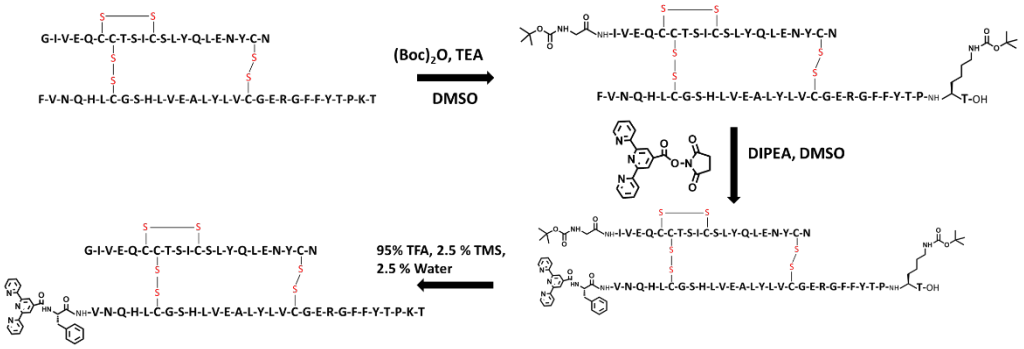

Scheme S2: Synthetic scheme for the synthesis of Phe^{B1}Tpy-HI

Synthesis of Gly^{A1}*Boc*-Lys^{B29}*BOC*-HI:

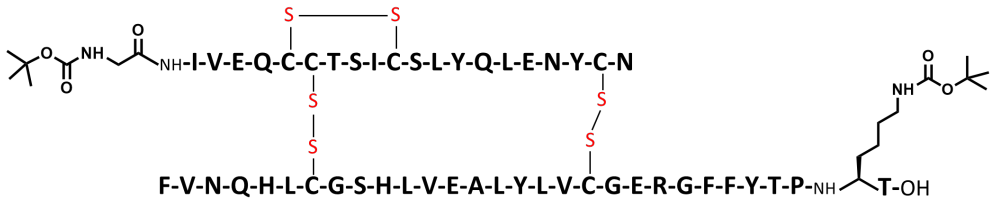

Scheme S3: Chemical Structure of Gly^{A1}*Boc*-Lys^{B29}*Boc*-HI

Synthetic procedure: A solution of $(Boc)_2O$ (17 mg, 0.077 mmol) in DMSO (50 µL), 20 µL of triethylamine, and 18 mg of N-hydroxysuccinimide in DMSO (0.2 mL) was mixed for 20 min. This solution of activated Boc- formed *in situ* was added in three portions at intervals of 3 min to a rapidly stirred solution of human insulin (200 mg, 0.034 mmol) in 4 mL of DMSO containing 5% triethylamine. Reaction was monitored by LCMS. The reaction mixture was diluted with water and product was isolated by Isolera, applying C18 column (Biotage Ultra C18, 20 um, 50 g). CH_3CN/H_2O mixed with 0.1% formic acid was used as eluents at a linear gradient of 40-60 % CH_3CN over 20 minutes, and a flow rate of 50 mL/min. Each fraction was analyzed using LCMS. Pure fractions were collected, CH_3CN were removed at reduced pressure at rotatory evaporator, followed by lyophilized to give product as a white powder (Di-BocHI-Yield: 98 mg, 48 %, Tri-Boc-HI-15 mg, 7.2 %).

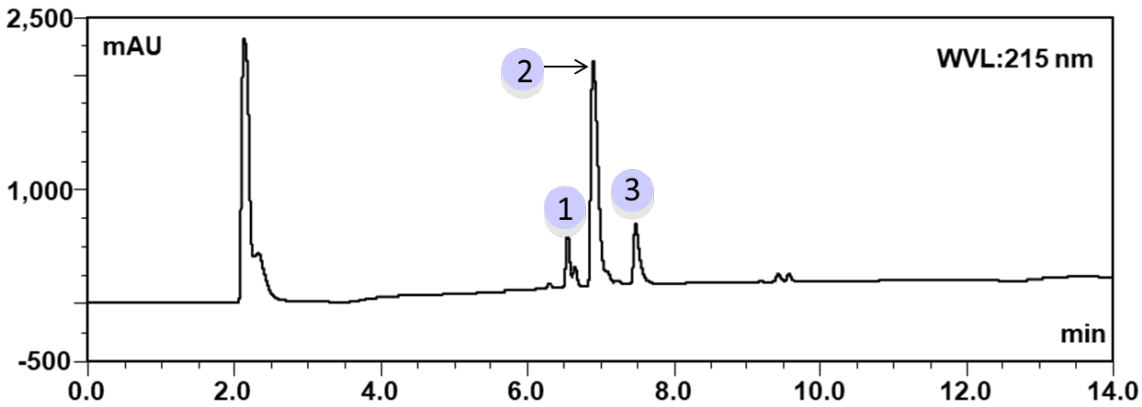

Figure S4: LCMS Chromatogram of crude from reaction of HI with Boc-anhydride. **Peak 1** corresponds to unreacted human insulin and monosubstituted insulin, **Peak 2** correspond to Di-Boc-HI, **Peak 3** corresponds to Tri-Boc-HI

LCMS Details: Molecular Formula of Gly^{A1}-*Boc*-Lys^{B29}*Boc*-HI ($C_{267}H_{399}N_{65}O_{81}S_6$)**: Calculated:** 6006.75

Calculated $[M+3H]^{3+}$: 2003.25, $[M+4H]^{4+}$: 1502.44, $[M+5H]^{5+}$: 1202.15, $[M+6H]^{6+}$: 1002.13.
Observed $[M+3H]^{3+}$: NO, $[M+4H]^{4+}$: 1502.0, $[M+5H]^{5+}$: NO, $[M+6H]^{6+}$: NO.

LCMS Details of Gly^{A1}*Boc*-Phe^{B1}*BOC*-Lys^{B29}*Boc*-HI ($C_{272}H_{407}N_{65}O_{83}S_6$) **Calculated:** 6108.80
Calculated: $[M+3H]^{3+}$: 2036.27, $[M+4H]^{4+}$: 1527.45, $[M+5H]^{5+}$: 1222.16, $[M+6H]^{6+}$: 1018.60.
Observed: $[M+3H]^{3+}$: NO, $[M+4H]^{4+}$: 1527.30, $[M+5H]^{5+}$: 1222.1, $[M+6H]^{6+}$: NO.

Table S2: LCMS analysis of DiBoc-HI			
Serial No.	**Peak**	**Calculated**	**Observed**
1.	$[M]^+$	6005.74	Not Observed
2.	$[M+H]^+$	6006.75	Not observed
3.	$[M+2H]^{2+}$	3003.89	Not observed
4.	$[M+3H]^{3+}$	2003.25	Not observed
5.	$[M+4H]^{4+}$	1502.44	1502.0
6.	$[M+5H]^{5+}$	1202.15	1214.9
7.	$[M+6H]^{6+}$	1002.13	Not Observed

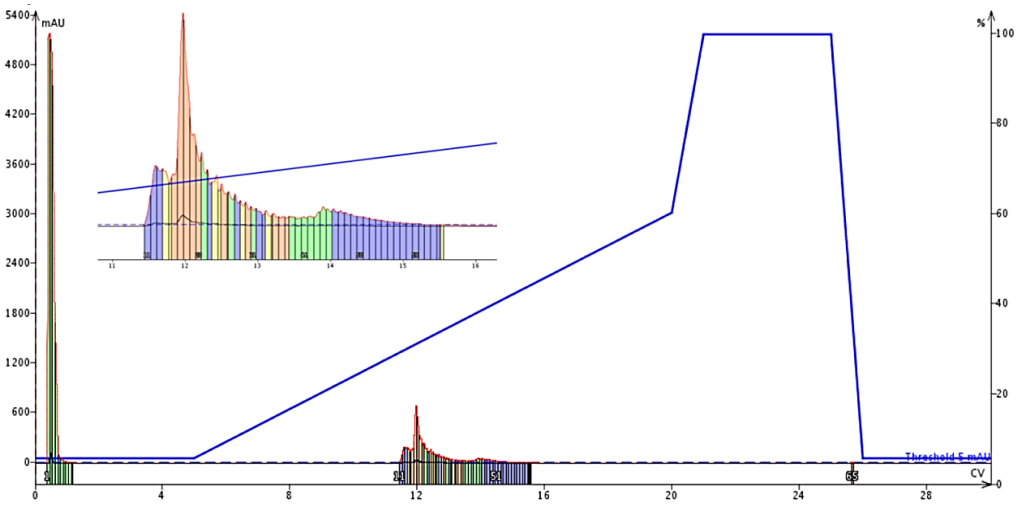

Figure S5: HPFC chromatogram for the purification Gly^{A1}*Boc*-Lys^{B29}*Boc*-HI

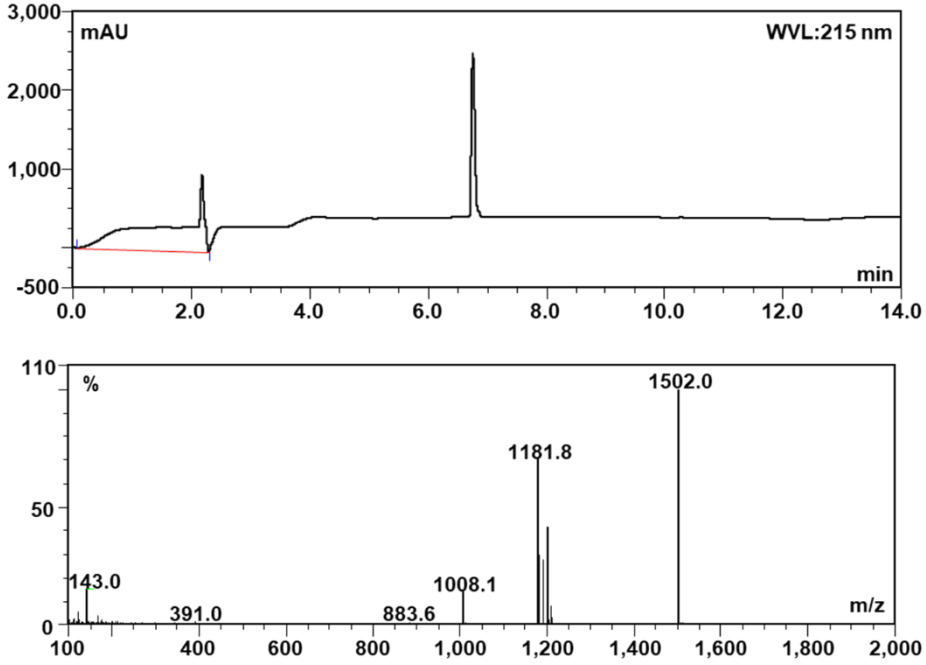

Figure S6: LCMS chromatogram and mass spectrum of Gly^{A1}*Boc*-Lys^{B29}*BOC*-HI after purification

V8 enzymatic analysis of Gly^{A1}*Boc*-Lys^{B29}*BOC*-HI:

- Gly^{A1}-*Boc*-Glu^{A4} ($C_{23}H_{40}N_4O_9$) **Calculated** $[M+H]^+$: 517.2868, **Observed**: 517.2735
- Gln^{A5}-Glu^{A17}+ Phe^{B1}-Glu^{B13} ($C_{126}H_{194}N_{34}O_{41}S_4$) **Calculated** $[M+2H]^{2+}$: 1485.160, **Observed**: 1485.1210, **Calculated** $[M+3H]^{3+}$: 990.4425, **Observed**: 990.4185.
- Asn^{A18}-Asn^{A21} + Ala^{B14}- Glu^{B21} ($C_{59}H_{88}N_{14}O_{20}S_2$) **Calculated** $[M+H]^+$: 1377.581, $[M+2H]^{2+}$: 689.294, **Observed** $[M+H]^+$: 1377.5443, $[M+2H]^{2+}$: 689.2772.
- Arg^{B22}-Lys^{B29}-*Boc*-Thr^{B30} ($C_{74}H_{110}N_{14}O_{20}$) **Calculated** $[M+H]^+$: 1216.6361, **Observed**: $[M+H]^+$: 1216.6032.

Synthesis of Gly^{A1}*Boc*-Lys^{B29}*Boc*-Phe^{B1}-2,2':6',2"-terpyridine-4'-carbamide-HI:

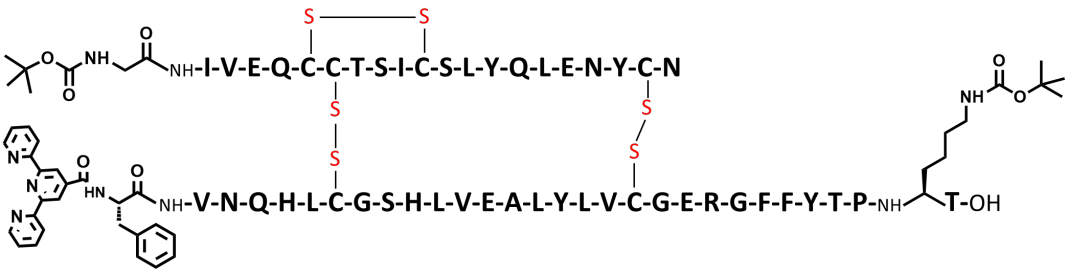

Scheme S4: Chemical Structure of Gly^{A1}*Boc*-Lys^{B29}*Boc*-Phe^{B1}*Tpy* -HI

Synthetic procedure: A mixture of 120 mg (0.0199 mmol) of Gly^{A1}-*Boc*-Lys^{B29}-*Boc*-HI (DiBoc-HI) and 9.7 mg (0.026 mmol) of terpyridine-NHS ester in 2.0 mL of DMSO containing 5% triethylamine (by volume) was stirred for 10 minutes at ambient temperature. After that, the reaction was monitored by LCMS at different time points (10, 20, 30, 40 min), which confirmed that reaction was complete within 10 min. The product was isolated with an Isolera instrument on a C18 column (Biotage Bio C18 20 um 50 g). CH_3CN/H_2O mixed with 0.1% formic acid was used as eluents at a linear gradient of 5-50

% CH_3CN over 20 minutes, and a flow rate of 50 mL/min. Fractions were combined, CH_3CN removed at reduced pressure on a rotatory evaporator, followed by lyophilization to give the product as a white powder (Yield: 91.0 mg, 72.8 %).

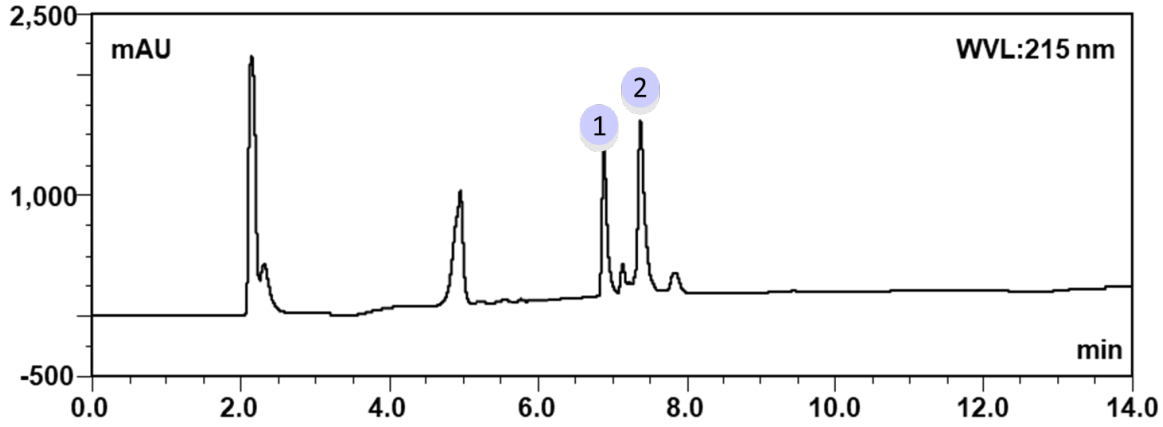

Figure S7: LCMS chromatogram for the reaction of Gly^{A1}*Boc*-Lys^{B29}*Boc*-HI with Tpy-NHS ester. **Peak 1** corresponds to the starting material Di-Boc-Hi and **peak 2** corresponds to the formation of product.

LCMS Details: Molecular Formula of Gly^{A1}*Boc*-Lys^{B29}*Boc-Phe^{B1}Tpy*-HI ($C_{283}H_{408}N_{68}O_{82}S_6$)**: Calculated:** 6264.823.
Calculated: $[M+3H]^{3+}$: 2089.61, $[M+4H]^{4+}$: 1567.21, $[M+5H]^{5+}$: 1254.17, $[M+6H]^{6+}$: 1045.14.
Observed: $[M+3H]^{3+}$: NO; $[M+4H]^{4+}$: 1566.70, $[M+5H]^{5+}$: 1253.60.0, $[M+6H]^{6+}$: NO.

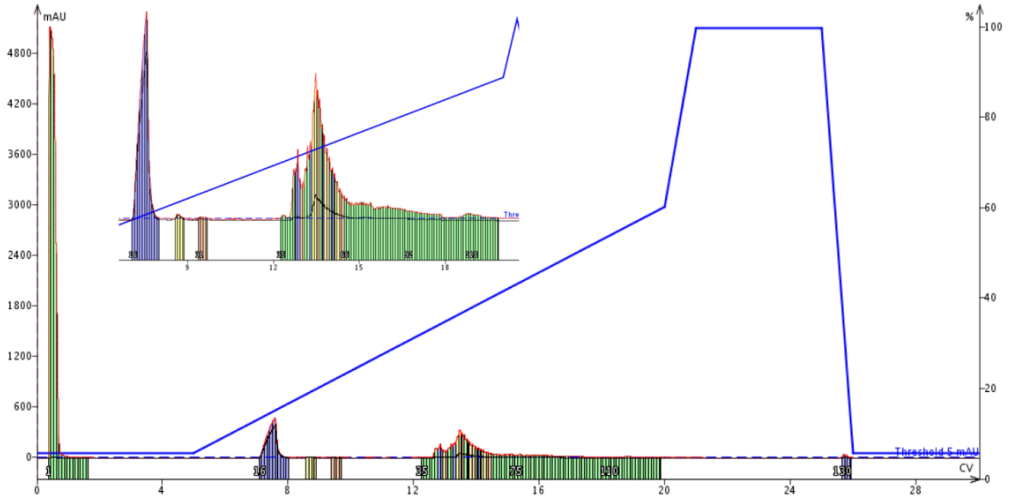

Figure S8: Isolera chromatogram for the purification of Gly^{A1}-*Boc*-Lys^{B29}-*Boc*-Phe^{B1}*Tpy*-HI.

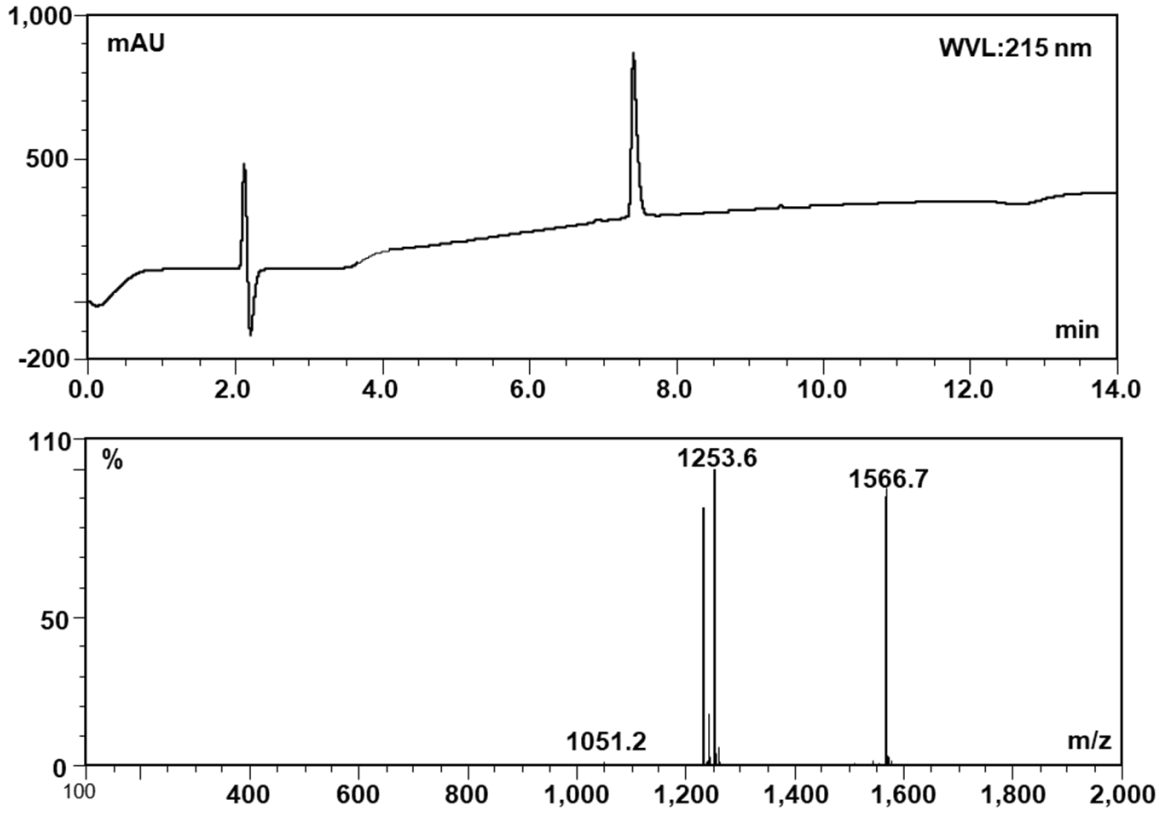

Figure S9: LCMS chromatogram and mass spectrum for Gly^{A1}*Boc*-Lys^{B29}*Boc*-Phe^{B1}*Tpy*-HI after purification.

V8 enzymatic analysis- of Gly^{A1}-*Boc*-Lys^{B29}*Boc-Phe^{B1}Tpy*-HI:

- **Gly^{A1}-*Boc*-Glu^{A4}**: ($C_{23}H_{40}N_4O_9$) **Calculated**: 516.28, **Observed**: 516.2
- **Gln^{A5}-Glu^{A17} + Phe^{B1}Tpy-Glu^{B13}** ($C_{142}H_{203}N_{37}O_{42}S_4$) **Calculated** $[M+2H]^{2+}$: 1615.19, **Observed**: 1615.20, **Calculated**: $[M+3H]^{3+}$: 1076.80, **Observed:** $[M+3H]^{3+}$: 1076.7.
- **Asn^{A18}-Asn^{A21} + Ala^{B14}-Glu^{B21}** ($C_{59}H_{88}N_{14}O_{20}S_2$) **Calculated** $[M+H]^+$: 1377.581, $[M+2H]^{2+}$: 689.294, **Observed**: 689.300**.**
- **Arg^{B22}-Lys^{B29}*Boc*-Thr^{B30} ($C_{54}H_{77}N_{13}O_{13}$) Calculated** $[M+H]^+$: 1216.63, **Observed**: 1216.6.

Table S3: LCMS analysis of Gly^{A1}*Boc*-Lys^{B29}*Boc-Phe^{B1}Tpy*-HI

Serial No.	Peak	Calculated	Observed
1.	$[M]^+$	6262.814	Not Observed
2.	$[M+H]^+$	6263.824	Not observed
3.	$[M+2H]^{2+}$	3133.419	Not observed
4.	$[M+3H]^{3+}$	2089.616	Not observed
5.	$[M+4H]^{4+}$	1567.213	1566.70
6.	$[M+5H]^{5+}$	1254.173	1253.60
7.	$[M+6H]^{6+}$	1045.145	Not Observed

Synthesis of Phe^{B1}-2,2':6',2"-terpyridine-4'-carbamide-human insulin:

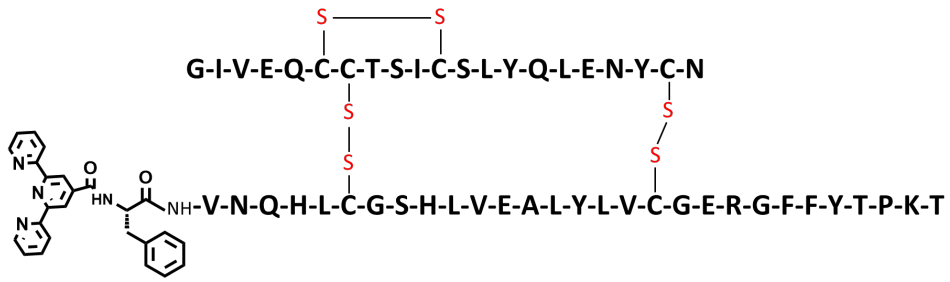

Scheme S5: Chemical Structure of Phe^{B1}*Tpy* -HI

Synthetic procedure: Gly^{A1}*Boc*-Lys^{B29}*Boc-Phe^{B1}Tpy*-HI (90 mg, 0.014 mmol) was treated with a mixture of 95% TFA and 2.5 % water and 2.5 % Trimethysilane for 1 hour. The reaction was monitored by LCMS. After 1h, TFA was removed under a stream of nitrogen. The product was further washed by dry ethyl ether to remove any soluble organic impurities and dried under high vacuum to yield a fine white powder. The product was further purified with an Isolera on a C18 column (Biotage Bio C18 20 um 50 g). CH_3CN/H_2O mixed with 0.1% formic acid was used as eluents at a linear gradient of 5-50% CH_3CN over 20 minutes, and a flow rate of 50 mL/min. Each fraction was analyzed through LCMS. Pure Fraction were combined, CH_3CN were removed at reduced pressure on a rotatory evaporator, followed by lyophilization to give a white powder (Yield 41 mg, 47 %).

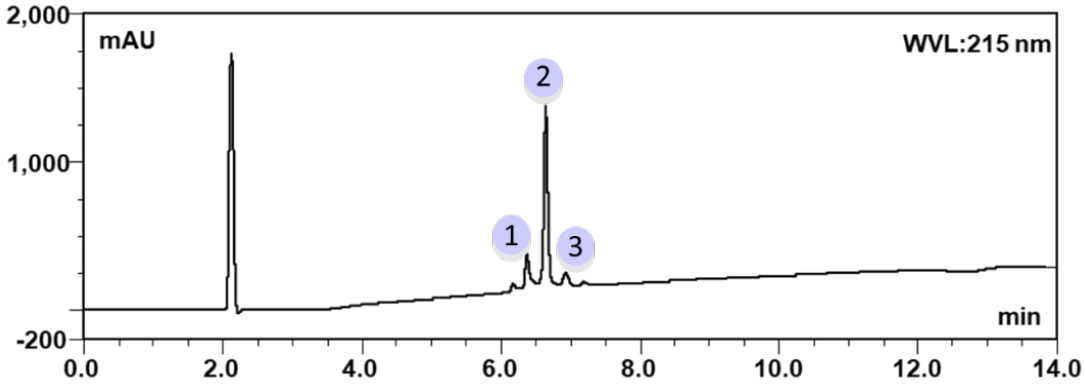

Figure S10: LCMS Chromatogram for crude of Phe^{B1}*Tpy*-HI, **Peak 1 and 3** corresponds to impurity and **peak 2** relates to Phe^{B1}*Tpy*-HI.

LCMS Details: Molecular Formula of Phe^{B1}*Tpy*-HI ($C_{273}H_{392}N_{68}O_{78}S_6$)**: Calculated:** 6062.71
Calculated: $[M+3H]^{3+}$: 2022.58, $[M+4H]^{4+}$: 1517.18, $[M+5H]^{5+}$: 1214.15, $[M+6H]^{6+}$: 1011.961.
Observed: $[M+3H]^{3+}$: NO, $[M+4H]^{4+}$: 1517.0, $[M+5H]^{5+}$: 1214.0, $[M+6H]^{6+}$: 1012.0.

V8 analysis of Phe^{B1}-*2,2':6',2"-terpyridine-4'-carbamide-human insulin*:

- **Gly^{A1}-Glu^{A4}** ($C_{18}H_{32}N_4O_7$) **Calculated**: 416.22; **Observed**: Not Observed
- **Gln^{A5}-Glu^{A17} + Phe^{B1}*Tpy*-Glu^{B13}** ($C_{142}H_{203}N_{37}O_{42}S_4$) **Calculated** $[M+2H]^{2+}$: 1615.19, **Observed**: $[M+2H]^{2+}$: NO, **Calculated.** $[M+3H]^{3+}$: 1076.80, **Observed** $[M+3H]^{3+}$: 1076.80.
- **Asn^{A18}-Asn^{A21} + Ala^{B14}- Glu^{B21}** ($C_{59}H_{88}N_{14}O_{20}S_2$) **Calculated** $[M+H]^{+}$: 1377.581, $[M+2H]^{2+}$: 689.294, **Observed**: 1377.590, 689.300.
- **Arg^{B22}-Thr^{B30}** ($C_{54}H_{77}N_{13}O_{13}$) **Calculated** $[M+H]^{+}$: 1116.58, **Observed**: 1116.16, **Calculated** $[M+2H]^{2+}$: 558.79, **Observed**: 558.8

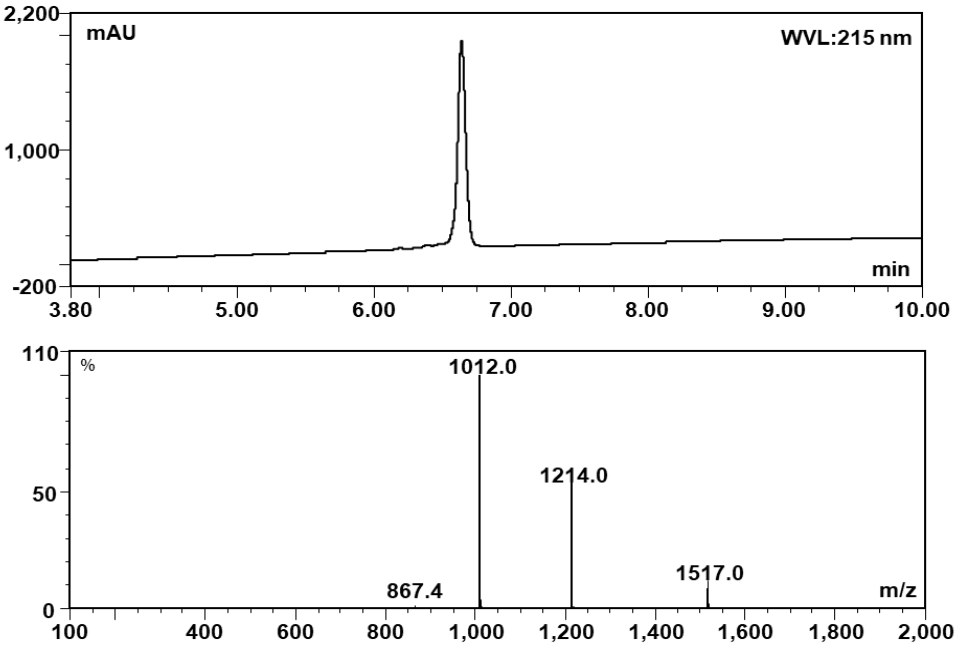

Figure S11: LCMS chromatogram and mass spectrum of Phe^{B1}Tpy-HI after purification.

Table S4: LCMS analysis of Phe^{B1}*Tpy*-HI			
Serial No.	**Peak**	**Calculated**	**Observed**
1.	$[M]^{+}$	6062.712	Not Observed
2.	$[M+H]^{+}$	6063.719	Not observed
3.	$[M+2H]^{2+}$	3033.367	Not observed
4.	$[M+3H]^{3+}$	2022.580	Not observed
5.	$[M+4H]^{4+}$	1517.187	1517.0
6.	$[M+5H]^{5+}$	1213.951	1214.0
7	$[M+6H]^{6+}$	1011.96	1012.0
8	$[M+7H]^{7+}$	867.39	867.40

1.4 Sample Preparation for UV-Vis, CD, Photoluminescence and SAXS Study:

(a) Stock solution of Lys^{B29}*Tpy*-HI and Human Insulin (HI):

Degassed MilliQ H_2O was added to LysB^{29}Tpy-HI/Human Insulin (around 8.0 mg of dry powder) separately and shaken gently for 2-3 minute, at which time it appeared as a suspension. The pH of solution was increased to pH 10.0 by addition of 0.2 M NaOH (added 2 µL for 2-3 times, if the pH rose to more than 10.5 then it was lowered with 0.2 M HCl) and shaken gently so that LysB^{29}Tpy-HI/HI dissolved, and the solution appeared transparent.

Afterwards, the solution pH was adjusted to pH 7.5-7.7 using 0.2 M HCl. The solution was further filtered into another Eppendorf tube through 0.2 µm syringe filters in order to remove any precipitate/aggregates. The concentration of Lys^{B29}Tpy/HI was further determined on a Nanodrop instrument. The molar absorption coefficient value for HI is 5734 $M^{-1}cm^{-1}$ (at 280 nm) while for Lys^{B29}Tpy-HI, it's value is 21583 $M^{-1}cm^{-1}$. After determination of concentration, stock solutions were stored in fridge at 4 °C and utilized for further experiments. The Zn^{2+}, Eu^{3+} solution was prepared in MilliQ H_2O whereas the Fe^{2+} solution was prepared in 0.1 M HCl to prevent oxidation to Fe^{3+}. Stock solution of tris buffer had the concentration of 100 mM (pH 7.5).

(b) Sample preparation for Lys^{B29}Tpy-HI with Fe^{2+}:

The required amount of Lys^{B29}Tpy-HI/HI was taken from the stock solution in order to have its final concentration of 600 µM or 100 µM. Further, different equivalents of Fe^{2+}, which was dissolved in 0.1 M HCl to avoid oxidation of Fe^{2+} to Fe^{3+}, was added separately to Lys^{B29}Tpy-HI/HI solution at adjusted pH 2.5 and followed by increasing the pH to 7.5 using 0.2 M NaOH and addition of tris buffer from stock solution (pH 7.5, 100 mM) at its final conc. of 10 mM. All UV-Vis measurements were carried out on a JASCO V-650 Spectrophotometer. A characteristic absorbance band at 570 nm appeared with the formation of the charge transfer complex $Fe(Lys^{B29}Tpy\text{-}HI)_2^{2+}$. There is no such band appears for the reference samples of HI with Fe^{2+}. With the increasing equivalents of Fe^{2+} in Lys^{B29}Tpy-HI, the band at 570 nm enhanced accordingly. Increasing equivalents of Fe^{2+} beyond 1/3 caused precipitation after 2-3 hours. Thus, experiments with higher equivalents of Fe^{2+} were not pursued.

(c) Sample preparation for Lys^{B29}Tpy-HI with Eu^{3+}:

The required amount of Lys^{B29}Tpy-HI/HI was taken from the stock solution in order to have a final concentration of 600 µM. Further, different equivalents of Eu^{3+} was added at pH 10.0 separately followed by decreasing the pH to 7.5 using 0.1 M HCl and addition of the required amount of tris buffer from stock solution (100 mM, pH 7.5) so that its final concentration was 10 mM. Further, the pH of the solution was maintained at 7.5. Due to complexation between terpyridine and Eu^{3+}, there was a shift in the absorbance of terpyridine from 327 nm to 350 nm. There was no such absorbance band for the reference samples of HI with Eu^{3+}. With the increasing equivalents of Eu^{3+} in Lys^{B29}Tpy-HI, the band at 350 nm enhanced accordingly. Increasing equivalents beyond 1/3 leads to precipitation after 24 hours. This observation allowed us not to pursue the experiments with higher equivalents of Eu^{3+}.

(d) Sample preparation for Lys^{B29}Tpy-HI/HI with Fe^{2+} and Zn^{2+}:

The required amount of Lys^{B29}Tpy-HI/HI was taken from the stock solution in order to have a final concentration of 100 µM. Further, different equivalents of Fe^{2+} which was dissolved in 0.1 M HCl to avoid oxidation of Fe^{2+} to Fe^{3+}, was added separately to Lys^{B29}Tpy-HI solution at pH 2.5 and followed by increasing the pH to 4.0 using 0.2 M NaOH, addition of the required equivalent of Zn^{2+} and followed by tris buffer (at its final conc. of 10 mM), while the pH was

maintained at 7.5. UV-Vis measurements were carried out on a JASCO V-650 Spectrophotometer. A characteristic absorbance band at 570 nm appears with the formation of the charge transfer complex $Fe(Lys^{B29}Tpy\text{-}HI)_2^{2+}$. There was no such absorbance band for the reference samples of HI with Fe^{2+} and Zn^{2+}. With the increasing equivalents of Fe^{2+} in Lys^{B29}Tpy-HI, the band at 570 nm enhanced accordingly. Increasing equivalents of Fe^{2+} and Zn^{2+} beyond ¼ leads to precipitation after to 2-3 hours. That was the reason for us to not execute the experiment with higher equivalent of Fe^{2+} and Zn^{2+}. Selected samples were analyzed through UV-Vis, DLS and CD, which did not have precipitation characteristics even after long duration of incubation.

(e) Sample preparation for Lys^{B29}Tpy-HI with Eu^{3+} and Zn^{2+}:

The complexation between metal and Lys^{B29}*Tpy*-HI/Human Insulin was performed under pH control. The required amount of Lys^{B29}*Tpy*-HI was taken from the stock solution in order to have a final concentration of 100 µM. Further, different equivalents of Eu^{3+} were added at pH 10.0 separately followed by decreasing the pH to 8.0 using 0.1 M HCl and added required amount of Zn^{2+} and followed by tris buffer from stock solution (100 mM, pH 7.5) at its final concentration of 10 mM. The pH was maintained at 7.5.

Due to complexation between terpyridine and Eu^{3+}, there is shifting in the absorbance of Terpyridine- from 327 nm to 350 nm. There was no such absorbance band for the reference samples of HI with Eu^{3+} and Zn^{2+}. With the increasing equivalents of Eu^{3+} in Lys^{B29}Tpy-HI, the band at 350 nm enhanced accordingly. Increasing equivalents beyond 1/3 leads to precipitation after 24 hours. This observation allowed us not to execute the experiments with higher equivalents of Eu^{3+}. Selected samples were analyzed through UV-Vis, DLS and CD, which did not have precipitation behaviour even after long during of incubation.

(f) Sample preparation for *in vivo* studies: A stock solution of Lys^{B29}Tpy-HI or HI was prepared in sterile purified H_2O following the method mentioned in section 1.4.

Lys^{B29}*Tpy*-HI and HI samples: The required volume of Lys^{B29}Tpy-HI or HI was diluted from the stock solution separately for each sample to reach a final conc. of 6.0 µM (~0.0362 mg/mL). The required volume of tris buffer from stock solution (100 mM, pH 7.5) to get its final conc. of 10 mM and the required volume of sterile purified water were added to obtain a total volume of 1.2 mL, adjusted pH to 7.5 using 0.2M HCl (Concentration specified in Table S5).

For Fe^{2+} complexes: Calculated volumes of Lys^{B29}Tpy-HI or HI was taken from the stock solution, the pH was adjusted to 2-3 with 0.2 M HCl, and the calculated amount of the Fe^{2+} ion was added, followed by tris buffer from stock solution (100 mM, pH 7.5) at its final conc. of 10 mM and supplemented with sterile purified H_2O to provide a total volume of 1.2 mL. The pH was adjusted to pH 7.5 with 0.2 M NaOH. (concentration specified in Table S5).

For Eu^{3+} complexes: Calculated volumes of Lys^{B29}Tpy-HI or HI was taken from the stock solution, pH was adjusted to 10.0 with 0.2 M NaOH and the calculated volume of the Eu^{3+} was added, followed by required volume of tris buffer from the stock solution (100 mM Tris Buffer, pH 7.5) to get its final conc. of 10 mM. Then solution was supplemented with sterile purified H_2O to provide a total volume of 1.2 mL, final pH was adjusted to 7.5 using 0.2 M HCl (Concentration specified in Table S5).

Table S5: Sample details for in vivo studies			
Serial No	**Sample Name**	**Concentration**	**Volume**
1.	Lys^{B29}Tpy-HI alone	0.0362 mg/mL	1.2 mL
2.	Lys^{B29}Tpy-HI with 1/6 Fe^{2+}	0.0362 mg/mL	1.2 mL
3.	Lys^{B29}Tpy-HI with 1/12 Eu^{3+}	0.0362 mg/mL	1.2 mL
4.	Phe^{B1}Tpy-HI alone	0.0362 mg/mL	1.2 mL
5.	Phe^{B1}Tpy-HI with 1/6 Fe^{2+}	0.0362 mg/mL	1.2 mL
6.	Phe^{B1}Tpy-HI with 1/12 Eu^{3+}	0.0362 mg/mL	1.2 mL
7.	HI alone	0.0347 mg/mL	1.2 mL
8.	Tris buffer	10 mM pH 7.5	1.2 mL

2.0 Photoluminescence/Lifetime experiment and result:

The method for sample preparation for the photoluminescence and lifetime experiment was same as is described earlier. The photoluminescence and lifetime spectra were measured on a Cary Eclipse instrument in phosphorescence mode using a Xe flash lamp. The PMT voltage was set to 700V for both steady state and time-dependent measurements. In the Cary Scan application the excitation and emission slits were set at 20 nm and 2.5 nm and ten scans were averaged using a scan rate of 2000 nm/min and an averaging time of 2 msec with a data interval of 0.8 nm. The emission filter was set to 500 nm – 1100 nm and the excitation wavelength was 350 nm with emission scanned from 560 nm – 720 nm. For sample preparation, required amount of Lys^{B29}Tpy-HI was taken from the stock solution to achieve the final conc. of Lys^{B29}Tpy-HI (600 µM) and added the different equivalents (1/24 to 1/3) of $EuCl_3 \cdot 6H_2O$ and $Eu(OTf)_3$ in H_2O and D_2O at pH 10.0, followed by Tris Buffer 10 mM in their respective solvent H_2O and D_2O accordingly at pH 7.5. Emission peaks at 583 nm, 592 nm, 616 nm, 652 nm, and 692 nm were observed.

Using the Cary Lifetime module, the time-dependent emission was recorded. The excitation and emission slits were set to 20 nm and 10 nm, respectively. The total decay time was set between 8 msec and 20 msec with up to 30 flashes and 20 cycles with a delay time of 0.100 msec and a gate time from 2 msec and down to 0.05 msec. The excitation wavelength was 350 nm and the emission was monitored at 619 nm. From the lifetime spectra of the Eu^{3+}-Lys^{B29}Tpy-HI Complex and use of the Horrocks equation, number of coordinated water molecules was calculated. The mathematical equation relates water coordination number to the measured differences in luminescence quenching between O-H and O-D oscillator, where q is the number of water molecules bound directly to the metal (inner-sphere) in 100% water; A is an empirically derived proportionality constant; $\tau_{H_2O}^{-1}$ and $\tau_{D_2O}^{-1}$ are the measured luminescence-decay rates in H_2O and D_2O.

Horrocks equation:

$$q = A\,(|\tau_{H_2O}^{-1} - \tau_{D_2O}^{-1}| - \alpha)$$

$$q = 1.2\,(|\tau_{H_2O}^{-1} - \tau_{D_2O}^{-1}| - 0.25)$$--------(In case of H_2O and D_2O A = 1.2 and α = 0.25)

Where q = number of water molecules directly bound to the metal in 100 % water
A is empirically derived proportionality constant
α = Represent quenching due to vibrational oscillator present outside of coordination sphere
τ_{H2O}^{-1} are τ_{D2O}^{-1} measured luminescence decay rate in H_2O and D_2O respectively.

Table S6:
Number of water molecules in coordination sphere calculated from Horrocks equation using lifetime spectra of Lys^{B29}Tpy-HI with $EuCl_3.6H_2O$

Component	Lifetime value in H_2O (T in ms)	τ_{H2O}^{-1}	Lifetime value in D_2O (T in ms)	τ_{D2O}^{-1}	q
Lys^{B29}Tpy-HI with 1/24 Eu^{3+}	0.38	2.63	2.05	0.487	2.33
Lys^{B29}Tpy-HI with 1/12 Eu^{3+}	0.38	2.63	1.93	0.518	2.28
Lys^{B29}Tpy-HI with 1/6 Eu^{3+}	0.38	2.63	1.73	0.576	2.21
Lys^{B29}Tpy-HI with 1/4 Eu^{3+}	0.38	2.63	1.86	0.536	1.88
Lys^{B29}Tpy-HI with 1/3 Eu^{3+}	0.38	2.63	1.85	0.540	2.25

Table S7:
Number of water molecules in coordination sphere calculated from Horrocks equation from lifetime spectra of Lys^{B29}Tpy-HI with different equivalent of $Eu(OTf)_3$.

Component	Lifetime value in H_2O (T in ms)	τ_{H2O}^{-1}	Lifetime value in D_2O (T in ms)	τ_{D2O}^{-1}	q
Lys^{B29}Tpy-HI with 1/24 Eu^{3+}	0.34	2.90	2.05	0.48	2.33
Lys^{B29}Tpy-HI with 1/12 Eu^{3+}	0.35	2.85	1.93	0.518	2.28
Lys^{B29}Tpy-HI with 1/6 Eu^{3+}	0.38	2.61	1.812	0.572	2.21
Lys^{B29}Tpy-HI with 1/4 Eu^{3+}	0.40	2.50	2.386	0.536	1.88
Lys^{B29}Tpy-HI with 1/3 Eu^{3+}	0.39	2.56	2.22	0.546	2.25

3.0 DLS study:

DLS measurement of Lys^{B29}Tpy-HI, HI alone and in presence of Fe^{2+} and Eu^{3+} was carried out on a Malvern Zetasizer μV instrument at 25℃ using a 2 microlitre Quartz cuvette with 1.25 mm light path length. Hydrodynamic radius was calculated using standard equation with dynamic viscosity of water at 25 °C which is embedded in Malvern program.

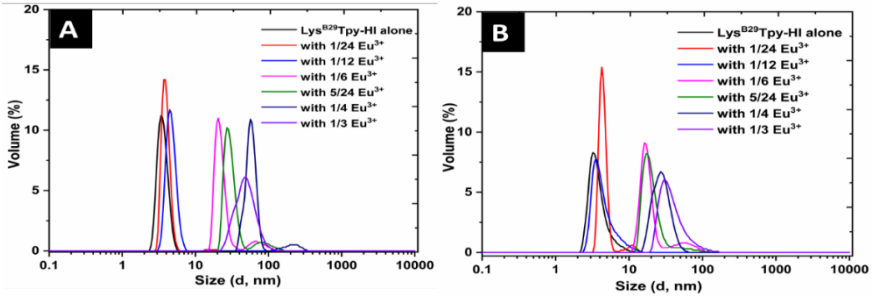

Figure S12: DLS measurements of Lys^{B29}Tpy-HI in different conc. with different equivalent of Eu^{3+} **(A)** 300 µM **(B)** 100 µM.

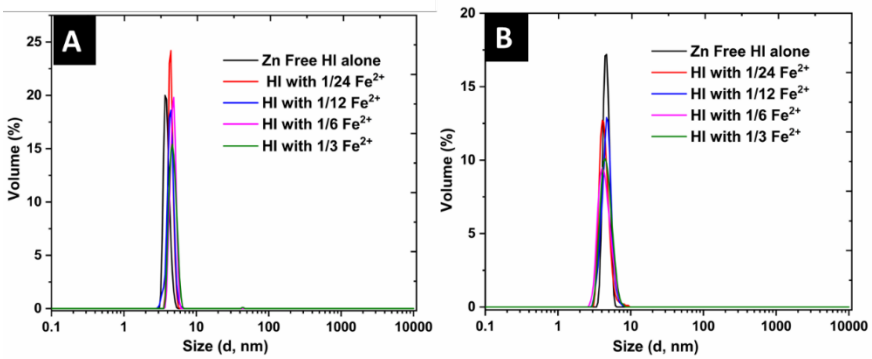

Figure S13: DLS measurements of HI with different equivalents of Fe^{2+} (A) 600 µM (B) 100 µM.

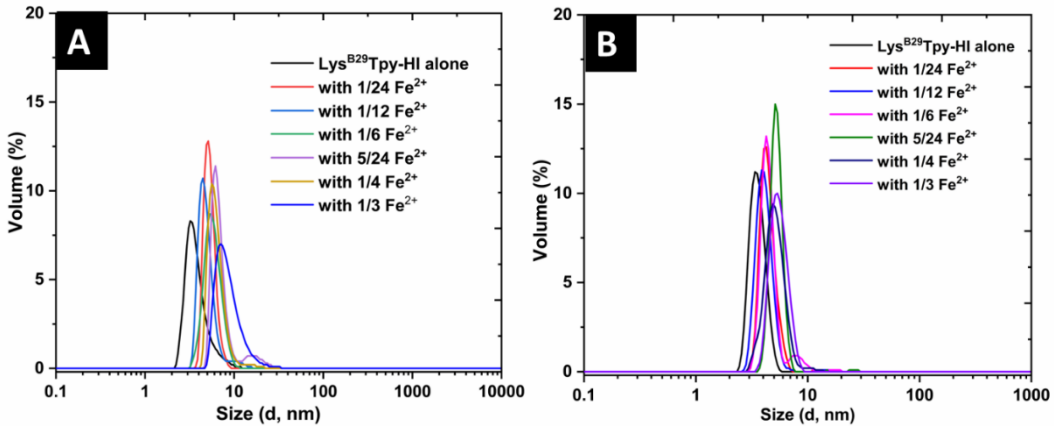

Figure S14: DLS measurements of Lys^{B29}Tpy-HI in different concentration with different equivalents of Fe^{2+} (A) 100 µM (B) 600 µM.

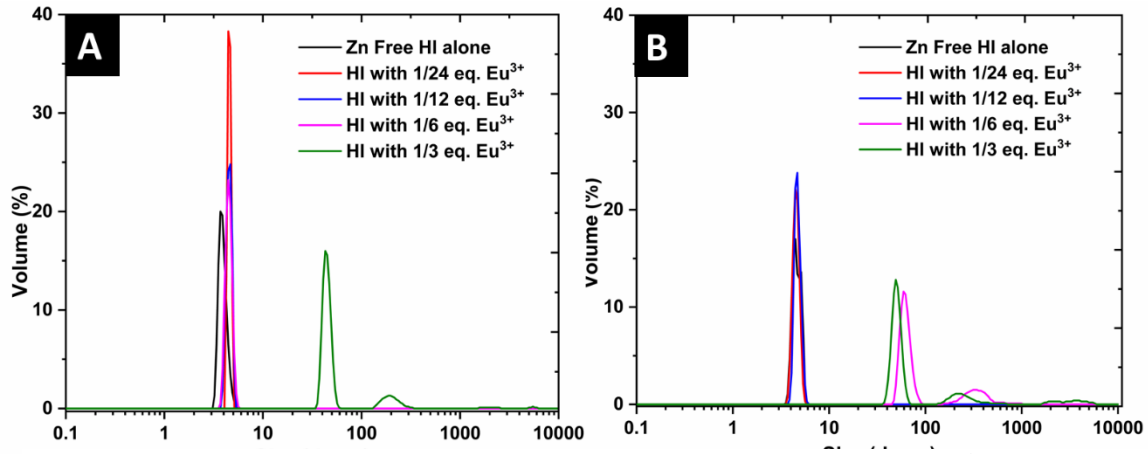

Figure S15: DLS measurements of Human Insulin (HI) in different concentration with Eu^{3+} (A) 100 µM (B) 600 µM.

4.0 SAXS methods and additional material:

4.1 SAXS experiments and data treatment:

SAXS experiments were undertaken at the EMBL beamline P12 at Petra III, Hamburg, Germany at T = 10°C, with a *q*-range of 0.0025 to 0.73 Å^{-1}. Buffer samples were measured before and after each macromolecular sample. The 40 µL sample volume was flowed through the beam to minimize radiation damage. 50 frames were collected per sample, with an exposure time of 95 ms/frame. Initial data reduction including azimuthal averaging and *q*-calibration were carried out at the beamline. The frames for each sample were compared in Primus[4] and frames with aberrant scattering were removed. The average scattering per sample was calculated from the remaining frames. The buffer sample measurements before and after each protein sample were averaged and subtracted from the latter. The data was absolute intensity scaled with water using Databsolute.[5] 2624 data points were rebinned into 119 points using a logarithmic coefficient of 1.04 with WillItRebin[6] Pair distance distribution functions were determined by Bayesian indirect Fourier transform with BayesApp[7] as implemented in BioXTAS RAW.[8] Molecular weight was estimated from the forward scattering *I*(0) using the relationship:[9]

$$\mathrm{MW} = \frac{N_\mathrm{A} I(0)}{c \cdot \Delta\rho_\mathrm{M}^2} \tag{1}$$

where *c* is the protein concentration, N_A is Avogadro's number, and the average excess scattering length density per unit mass of protein, $\Delta\rho_\mathrm{M}$, is given as:

$$\Delta\rho_\mathrm{M} = \frac{\rho_\mathrm{M,prot} - \rho_\mathrm{solv}\bar{\nu}}{r_0}, \tag{2}$$

where $r_0 = 2.8179 \times 10^{-13}$ cm is the scattering length of an electron, $\bar{\nu}$ is the partial specific volume of protein (set to the effective value of 0.7425 $\mathrm{cm^3 g^{-1}}$ suggested in ref[9b], $\rho_\mathrm{M,prot}$ is the number of electrons per unit mass of dry protein (3.22×10^{23} e $\cdot$ g^{-1})[9b], and ρ_solv is the number of electrons per unit volume of aqueous solvent (3.34×10^{23} e $\cdot$ cm^{-3}).

4.2 SAXS modelling:

The following describes two types of modelling used for analyzing SAXS data for discrete oligomers and extended (fractal) assemblies, respectively.

4.21 SAXS modelling of discrete oligomers:

Lys^{B29}Tpy-HI + Fe^{2+}: As discussed in the main text, SAXS for Lys^{B29}Tpy-HI with Fe^{2+} indicated moderate oligomerization with average SAXS-determined molecular weights of 36 and 55 kDa for 1/6 and 1/3 eq. Fe^{2+}, respectively. Thus, the sample with 1/3 eq. Fe^{2+} oligomerized to roughly 8 – 9 times the theoretical molecular weight of Lys^{B29}Tpy-HI (6.1 kDa). We therefore carried out molecular modeling to produce structures of this size, while at the same time incorporating some of the expected main modes of oligomerization, namely (i) dimerization via the native HI-dimer interface (assumed conserved in Lys^{B29}Tpy-HI) (ii) dimerization by two terpyridine moieties binding to the same Fe^{2+} (demonstrated spectroscopically) and (iii) other non-covalent association.

The starting point for SAXS modelling was a tetramer in which two Lys^{B29}Tpy-HI dimers (with native-HI-like dimerization inherited from the crystal structure 1UZ9.pdb) were coupled to a single, common Fe^{2+} via one terpyridine from each Lys^{B29}Tpy-HI dimer (Figure S16A), see Molecular Modeling section below.

Using FoxSDock[10] this tetramer was docked against its own copy using rigid body rotations and translations to maximize the fit to experimental SAXS data. The best resulting model is shown in Figure S16B (right) with fit to SAXS data shown in main article Figure 4F. Although the high-*q* region was not precisely estimated from the model, the overall fit was reasonable, and this model hence represents an estimate of the average solution structure.

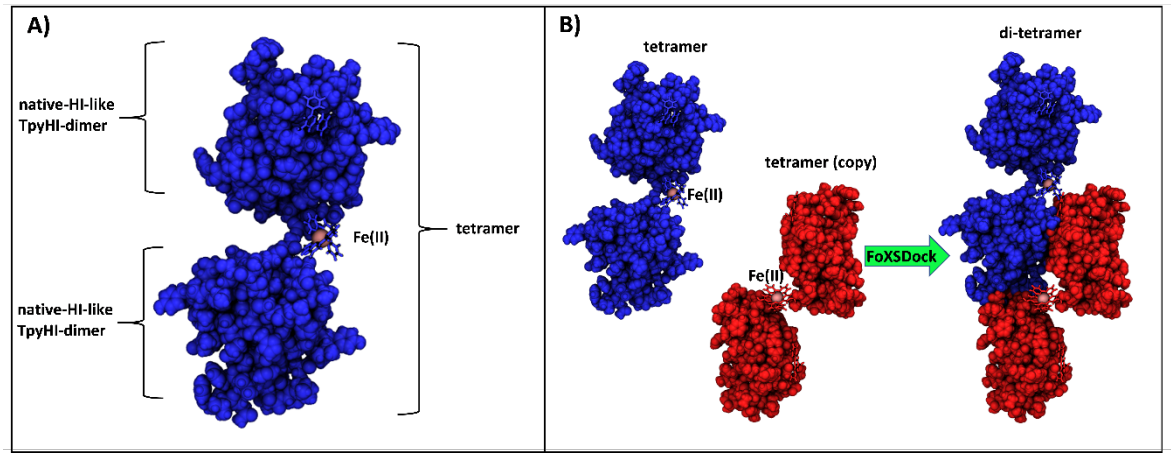

Figure S16: Molecular model for SAXS-predictions for Lys^{B29}Tpy-HI with 1/3 eq. Fe^{2+}. **(A)** Lys^{B29}Tpy-HI tetramer MD-relaxed structure. **(B)** Docking of two tetramers to optimize fit to SAXS data using FoXSDock. The shown di-tetramer structure is the same as shown in the main article Figure 4F, in a different representation.

4.22 SAXS modelling of fractal assemblies:

SAXS for both HI and Lys^{B29}Tpy-HI in the presence Eu^{3+} indicated fractal assemblies, which were analyzed within the framework of the Teixeira model[11] and later developments[12] as outlined in the following.

The SAXS intensity $I(q)$ from particles in solution where $q = 4\pi \cdot sin\theta/\lambda$ (2θ: scattering angle, λ: X − ray wavelength) can be written as the product of a form factor, $P(q)$, describing the intraparticle scattering, a structure factor, $S(q)$, describing the interparticle interactions and a prefactor, c, accounting for the particle concentration, molar mass and the second power of the excess scattering length per unit mass:

$$I(q) = c \cdot P(q) \cdot S(q)$$

At low sample concentrations $S(q) = 1$ can be assumed, allowing the expression:

$$I(q) = c \sum_i X_i \cdot P_i(q)$$

where X_i and $P_i(q)$ are the weight fraction and form factor, respectively, for oligomeric species *i*. Scattering from an oligomeric species *i* can further be expressed as the product: [12-13]

$$P_i(q) = p_i(q) \cdot f_i(q)$$

where $p_i(q)$ is the scattering from a single subunit (e.g. monomer) and $f_i(q)$ is a function describing the function of organizing the subunit into either a discrete oligomer (e.g. dimer, hexamer, etc.) or into an extended structure (e.g. fractal aggregates).

In this work, the form factor $p_i(q)$ and where appropriate $P_i(q)$ were calculated directly using CRYSOL[14] or FoXS[10] from molecular models based on crystal structures and simulations as described in the molecular modeling section below.

For fractal-like aggregates, the function $f_i(q)$ was modelled in the form:[11]

$$f_{frac}(q) = 1 + \frac{1}{(q \cdot r_0)^D} \frac{D \cdot \Gamma(D-1)}{\left[1 + \frac{1}{q^2 \cdot \xi^2}\right]^{\frac{D-1}{2}}} \cdot \sin\left[(D-1) \cdot \arctan(q \cdot \xi)\right]$$

where $r_0$is an interaction radius, D is the fractal dimension, $\Gamma(x)$ is the gamma-function, and ξ is the correlation length of the fractal domains. The model describes the structure of mass fractals of certain subunits in terms of the subunit size (r_0), characteristic size of individual fractal domains (ξ) and fractal dimension D_f. In this work f_{frac} was combined with a numerical form factor for molecular building units using a previously described approach[12, 3] and the decoupling approximation[15] accounted for the lack of subunit centrosymmetry. See also a more thorough discussion of the application of this model in relation to protein subunits in ref. [13]

The scattering for a mixture of fractal and non-fractal forms of a certain subunit *i* can then be written as:

$$I(q) = c\{X_i P_i(q) + X_{\mathrm{frac},i} F_{\mathrm{frac}}(q, P_i(q))\}$$

where $F_{\mathrm{frac}}(q, P_i(q))$ denotes the fractal model in combination with the form factor $P_i(q)$ for the relevant subunit, $X_{\mathrm{frac},i}$ is the weight fraction of subunit *i* in fractal form and $X_i = 1 - X_{\mathrm{frac},i}$ is the weight fraction of subunit *i* in non-fractal form.

In fitting the fractal model to SAXS data, the subunit size (r_0) was fixed to values measured in molecular models of the subunit while ξ and D_f were taken as fit parameters along with the fraction of subunits in fractals.

4.3 Molecular modeling for SAXS fitting:

The modeling of SAXS in this work relied on numerical form factors calculated from molecular models of plausible subunits for oligomeric species. We built these molecular models by editing and combining published crystal structures of insulins and terpyridine-metal complexes. Furthermore, we used key experimental observations as heuristics and constraints during modeling as described below.

4.31 Experimental constraints used in molecular modeling: A key experimental constraint discussed in the main article is the spectroscopic demonstration of the complexation of the terpyridine moiety of Lys^{B29}Tpy-HI with both Fe^{2+} and Eu^{3+} without secondary structure disruption. This strongly suggests that the interaction between metal ions and the terpyridine moiety contributed to oligomerization of Lys^{B29}Tpy-HI in formulations with Fe^{2+} and Eu^{3+}. We therefore explicitly included terpyridine-metal ions interactions in the relevant molecular models.

During modeling we took care not to disrupt other potential modes of self-assembly, such as association via the native insulin dimer-interface or metal-ion driven association via free carboxyl groups. This was particularly relevant for Eu^{3+} formulations where we expected that a representative oligomeric subunit should allow multiple orthogonal modes of self-assembly in order to be consistent with the fractal assemblies indicated by SAXS.

4.32 Lys^{B29}Tpy-HI dimerized via Tpy binding to Eu^{3+}: The simplest plausible metal-ion mediated oligomer was two copies of a Lys^{B29}Tpy-HI monomer dimerized via terpyridine complexation to Eu^{3+}. This structure was modelled by connecting an insulin monomer via the Lys^{B29} side-chain to each of the 4'-positions in a bis-Terpyridine-Eu^{3+} complex. The insulin monomer structure was chosen as the most representative structure in the NMR solution structure ensemble (PDB accession: 2JV1.pdb)[16] and the bis-terpyridine- Eu^{3+} complex was the crystal structure of bis(2,2':6',2''-Terpyridine-6-carboxylato) Eu^{3+} trifluoromethanesulfonate hemihydrate (CCDC accession: PABJOS)[17]. After merging these experimentally determined structures in Maestro (Schrödinger Release 2020-2: Maestro, Schrödinger, LLC, New York, NY, 2020) the resulting structure was edited to yield the assumed composition of the $[Eu(Lys^{B29}Tpy\text{-}HI)_2]^{3+}$ complex. Editing consisted of minor structural modifications and local relaxation, and included the replacement of the 6-carboxylato groups of the Eu^{3+} crystal complex with two water ligands in order to bring the structure into agreement with our experimental evidence for two waters coordinated to Eu^{3+}.

The structure was symmetrized to the nearest symmetry group (C2) to remove arbitrary asymmetries, giving the initial model shown in Figure S17A. The model was prepared for MD simulations in Desmond[18] (Desmond Molecular Dynamics System, D. E. Shaw Research, New York, NY, 2020. Maestro-Desmond Interoperability Tools, Schrödinger, New York, NY, 2020.) by assigning the OPLS3 force field[19] to all solute atoms and immersing the system in a cubic solvent box (10 Å buffer) of TIP3P[20] waters. The metal site geometry (Eu^{3+} and first coordination sphere atoms) was restrained during MD, and Fe^{2+} parameters were used for the metal ion since OPLS3 lacked Eu^{3+} parameters. Although deviating from the formal charge of +3 we assumed the Fe^{2+} parameters in this case provided more balanced simulation results by preventing excessive structural contraction around a high, localized charge. The overall system charge was neutralized by automatic addition of counterions and simulated under isobaric-isothermal conditions with Desmond default settings.

After 125 ns MD, the structure had relaxed to the stable conformation shown in Figure S17B. This MD-relaxed model retained approximate C2 symmetry and the dimer-interface residues (V12, F24, F25, Y26) remained solvent exposed. Thus, in addition to explicitly including the Tpy-Eu^{3+}-Tpy mediated dimerization, this model retained the possibility of native-like dimerization, see Figure S17D. The close-up view in Figure S17C shows that an Glu^{A4} side chain attracted to the metal center during MD, approximating a 9-coordinated metal site which is a possible coordination number for Eu^{3+}. All remaining Glu side chains were solvent-exposed and in principle available for metal-mediated cross-linking with other dimers (Figure S17E).

In summary, the $[Eu(Lys^{B29}Tpy\text{-}HI)_2]^{3+}$ molecular model built for SAXS predictions explicitly included Tpy-Eu^{3+}-Tpy dimerization and retained an unhindered native insulin dimer interface on both monomers as well as solvent exposed carboxyl groups (Glu side chains and terminal

COO^-). These features should allow branching of an oligomer composed of the subunit, consistent with the high fractal dimensions observed by SAXS. Importantly, the model produced convincing fits to the experimental SAXS data when used as a subunit for the SAXS modelling of fractals, as discussed below. However, in contrast to that system, the Fe^{2+} mediated dimer reorganized into a compact structure during MD, obstructing the native insulin dimer interfaces on each monomer, see Figure S17F and S17G.

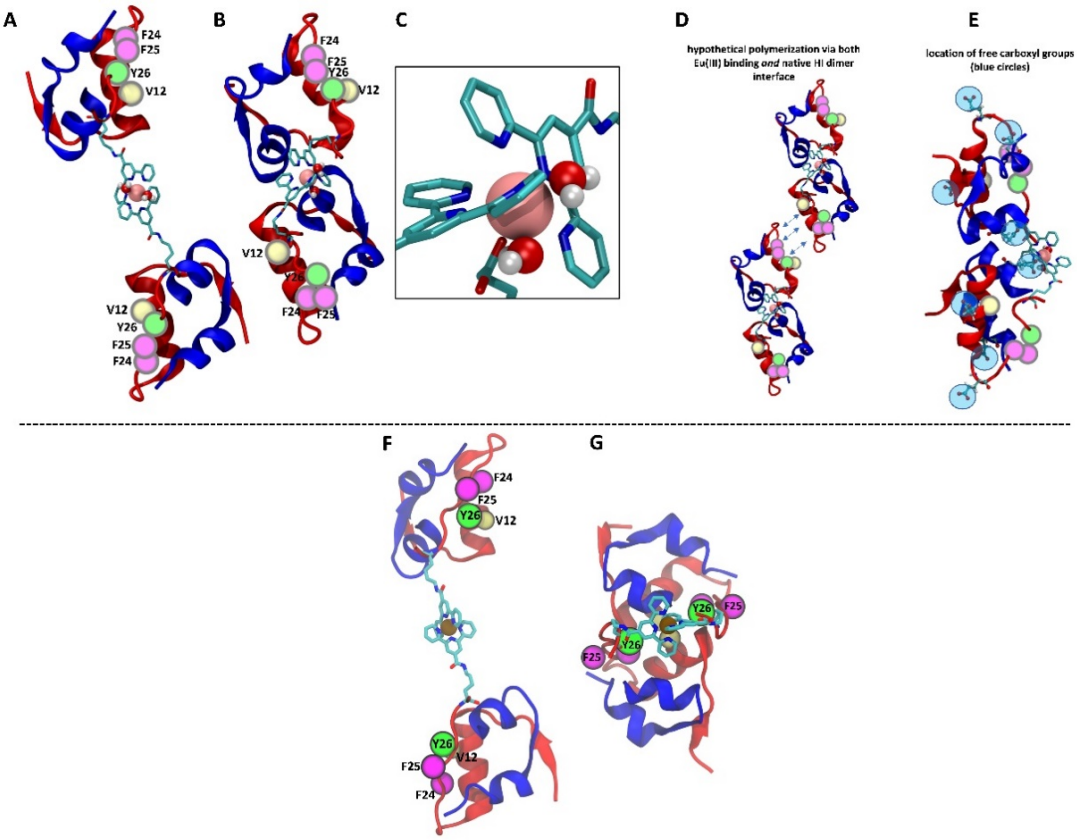

Figure S17. Top panel: Molecular modelling of the Lys^{B29}Tpy-HI Eu^{3+}-mediated dimer used for SAXS modelling. **(A)** Initial structure. **(B)** Structure after 125 ns MD. **(C)** Close-up of the MD-averaged Tpy metal binding site. **(D)** Hypothetical polymerization via both metal binding and native dimerization. Colored spheres labeled F24, F25, Y26, V12 indicate insulin dimer interface residues. **(E)** Rotated view of structure B showing the location of free carboxyl groups. **Bottom panel:** Molecular modelling of a Lys^{B29}Tpy-HI Fe^{2+}-mediated dimer. **(F)** Initial structure. **(G)** Structure after 125 ns MD. The compact structure after 125 ns buries the native dimerization interface. This structure was therefore not used for SAXS modeling.

.

4.33 Lys^{B29}Tpy-HI dimerized via Tpy binding to Fe^{2+}: We used the following experimental constraints to guide the modelling of an oligomeric subunit for Lys^{B29}Tpy-HI formulated with Fe^{2+}: The $I(q)$ plateau at low q at 1/3 eq. Fe^{2+}, showing that this system formed a discrete assembly. In addition, our spectroscopic studies showed the coordination of Fe^{2+} to Tpy in analogy to the samples formulated with Eu^{3+}.

We modelled the Tpy-Fe^{2+}-Tpy part of the complex using the crystal structure of bis(4'-(pyridin-4-ylethynyl)-2,2':6',2''-terpyridine)-Fe(III) tris(tetrafluoroborate) chloroform methanol

solvate (CCDC accession: XECZIR). We then built and MD simulated a Fe^{2+} mediated Lys^{B29}Tpy-HI dimer as described above for the Eu^{3+} mediated dimer. However, in contrast to that system, the Fe^{2+} mediated dimer reorganized into a compact structure during MD, obstructing the native insulin dimer interfaces on each monomer. Although this is a possible dimeric species, we also wanted to model the situation where the native dimerization interface was unobstructed, allowing the Fe^{2+} mediated dimer to further oligomerize via this interface.

To conserve the native dimerization interface during MD, we therefore built another initial model consisting of two native-like insulin hexamers instead of monomers. Since HI-hexamers do not dissociate in MD simulations, the native dimerization interface is guaranteed to be preserved.

This model was built by first editing the crystal structure of hexameric lithocholyl insulin (PDB-ID: 1UZ9)[21] to give a Lys^{B29}Tpy-HI hexamer using Maestro (Schrödinger Release 2020-3: Maestro, Schrödinger, LLC, New York, NY, 2020.). A dimer of this hexamer formed via Fe^{2+} bound to a single terpyridine on each hexamer was built by coupling to the bis-Tpy-Fe^{2+} complex from (CCDC accession XECZIR). The dimer of hexamers was subjected to MD simulation using the same protocol as for the $[Eu(Lys^{B29}Tpy\text{-}HI)_2]^{3+}$ model described above.

After 125 ns MD equilibration the part of the MD trajectory corresponding to the tetramer shown in Figure S16A was extracted. This tetrameric model was then used as a subunit for modelling the SAXS data for Lys^{B29}Tpy-HI + 1/3 eq. Fe^{2+} as described in the section on SAXS modelling above.

4.4 Supplementary SAXS results:

***4.41 Lys^{B29}Tpy-HI and HI without metal ions*:** SAXS intensities for Lys^{B29}Tpy-HI and HI were overall similar (Figure S18A). Comparison of the pair distance distribution functions (Figure S18B) also suggests similar oligomer ensembles, although Lys^{B29}Tpy-HI gave somewhat smaller structures (~13 kDa) compared to native HI (~18 kDa).

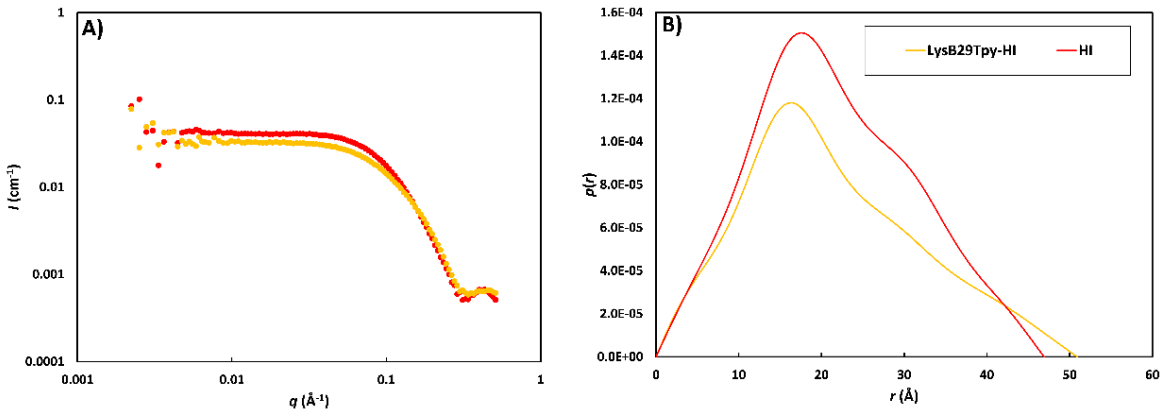

Figure S18: SAXS intensity **(A)** and pair distance distribution functions **(B)** for LysB29Tpy-HI (orange) and HI (red) at 600 µM. Average molecular weights calculated from *I*(0) were 18 kDa for HI and 13 kDa for LysB29Tpy-HI.

4.42 HI with Fe^{2+}: SAXS intensities (Figure S18A) and pair distance distribution functions (Figure S18B) indicated some additional oligomerization for HI with 1/3 eq. Fe^{2+} compared to HI without metal. The average molecular weights calculated from *I*(0) were 18 kDa for HI and 50 kDa for HI + 1/3 eq. Fe^{2+} .

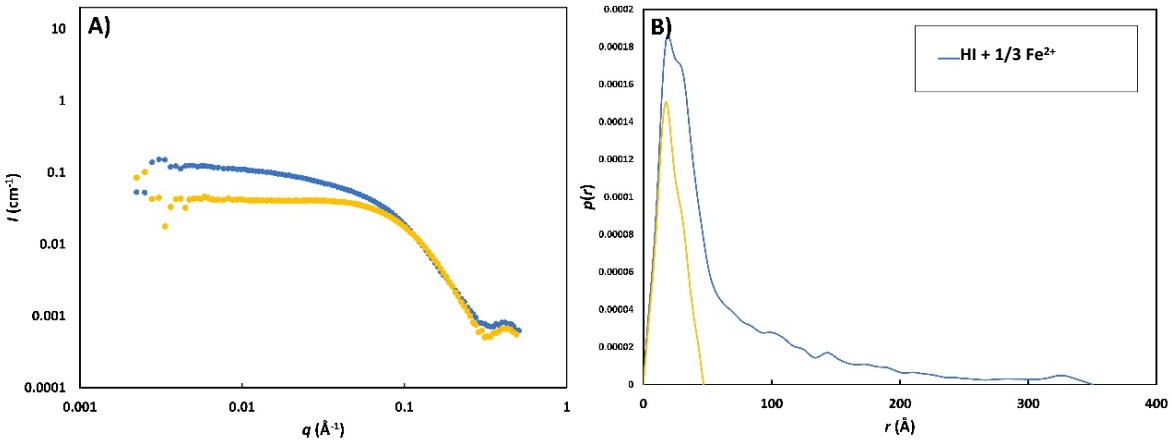

Figure S19. SAXS intensity **(A)** and pair distance distribution functions **(B)** for HI (orange) and HI + 1/3 eq. Fe^{2+} (blue) at 600 µM. Average molecular weights calculated from *I*(0) were 18 kDa for HI and 50 kDa for HI + 1/3 Fe^{2+}

4.43 HI with Eu^{3+}: SAXS data for HI with 1/3 eq. Eu^{3+} and 1/4 eq. Eu^{3+} indicated formation of large, fractal aggregates (Figure S20). We propose that the underlying attractive insulin-insulin interactions may be mediated by Eu^{3+} binding to insulin Ca^{2+} binding sites.[8]

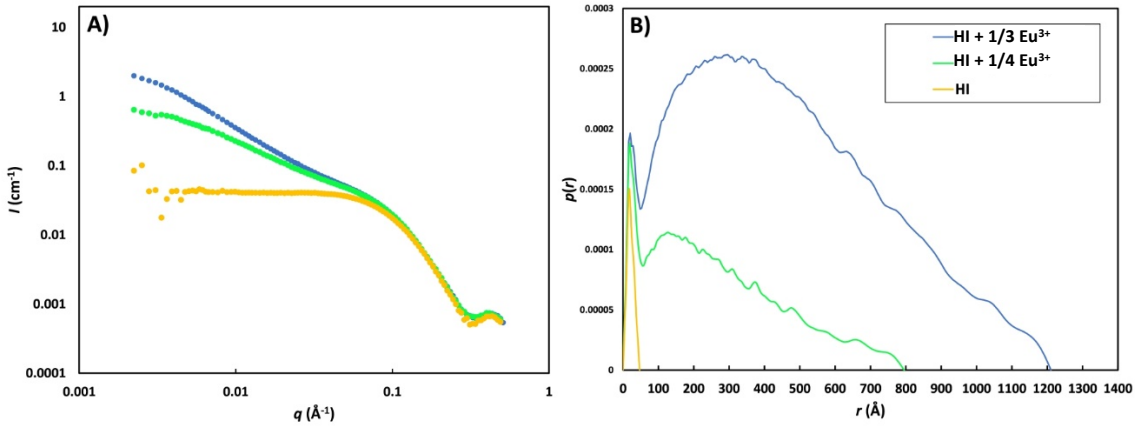

Figure S20. SAXS intensity **(A)** and pair distance distribution functions **(B)** for HI (orange), HI + 1/4 eq. Eu^{3+} (green), and HI + 1/3 eq. Eu^{3+} (blue) at 600 µM.

4.5 Fractal Modeling Results:

4.51 Fractal models for Lys^{B29}Tpy-HI + Eu^{3+}: A suitable subunit for fractal modelling was the LysB29Tpy-HI dimer formed by two Lys^{B29}Tpy-HI monomers coordinating a single Eu^{3+} via the terpy moieties (Figure S17B). This model had an approximate radius of 21 Å, which was fixed during fractal fitting to the SAXS data. Fits were obtained by combining the scattering from two species, the Eu^{3+}-mediated Lys^{B29}Tpy-HI dimer and fractals of this dimer:

$$I(q) = c\{X_{TpyHI-dimer}P_{TpyHI-dimer}(q) + X_{frac,TpyHI-dimer}F_{frac}(q, P_{TpyHI-dimer}(q))\}$$

SAXS data with fits are shown in Figure 4C. Key fractal parameters (r, ξ, D_f) are illustrated for the sphere fractal structures in Figure S21.

Table S8. Parameters for fractal modelling of SAXS data for Lys^{B29}Tpy-HI formulated with Eu^{3+}. The fitted parameters are: Fraction of subunit on fractal form (X_{frac}), fractal dimension (D_f), and fractal correlation length (ξ). Error estimates are given in parentheses.

Metal ion eq.	X_{frac}	D_f	ξ [Å]
1/6 Eu^{3+}	0.15 ($5\cdot10^{-3}$)	2.27 ($3\cdot10^{-2}$)	223 (10)
1/4 Eu^{3+}	0.34 ($3\cdot10^{-3}$)	2.38 ($2\cdot10^{-3}$)	200 (1)
1/3 Eu^{3+}	0.36 ($5\cdot10^{-3}$)	2.66 ($9\cdot10^{-4}$)	158 (2)

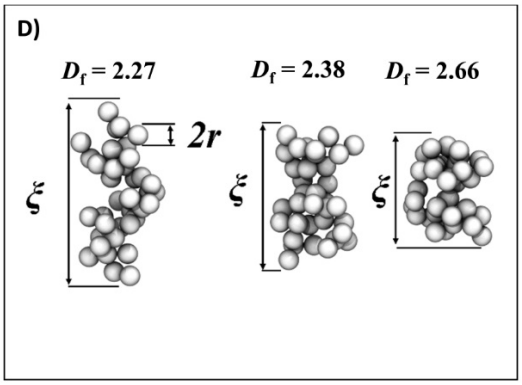

Figure S21: Sphere models of fractals consistent with fractal dimension from Teixeira models of SAXS data for Lys^{B29}Tpy-HI formulated with Eu^{3+}. Each model contains 39 spheres with r = 21 Å.

***4.52 Fractal models for of HI + Eu^{3+}*:** $I(q)$ and $p(r)$ for human insulin formulated with Eu^{3+} are shown in Figure S21A and S21B, respectively. The native human insulin dimer was used as subunit in fractal modelling, and the SAXS data could be modelled assuming a two-component mixture of native insulin dimers and fractals of dimers:

$$I(q) = c\{X_{HI-dimer}P_{HI-dimer}(q) + X_{frac,HI-dimer}F_{frac}(q, P_{HI-dimer}(q))\}$$

The resulting fractal model fits are shown in Figure S23 with parameters in Table S9.

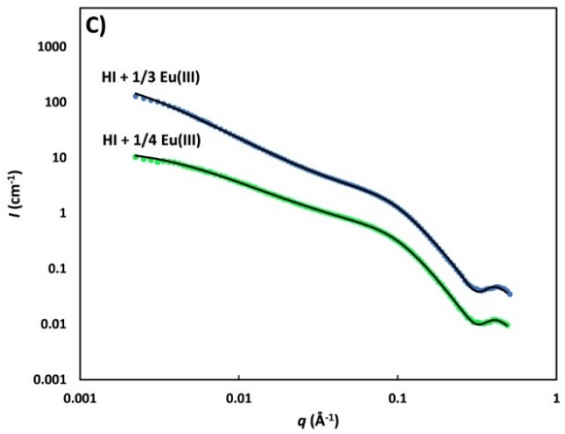

Figure S22: SAXS results for human insulin formulated with Eu^{3+}. Fractal fits. For visualization, the data have been scaled by 4^n where n = 1 - 2.

Relative to the corresponding samples with Lys^{B29}Tpy-HI the fits (Figure S22) gave lower fractal dimensions (1.36 for 1/4 Eu^{3+}, 1.59 for 1/3 Eu^{3+}) indicating less branched and more elongated fractals with larger fractal domains indicated by the correlation lengths (ξ =323 Å and 603 Å, respectively). Also, more insulin (71 – 72%) was predicted to be in fractal form relative to Lys^{B29}Tpy-HI.

Thus, the SAXS data and fractal models support that human insulin with Eu^{3+} assembles both qualitatively and quantitatively different than the corresponding samples of Lys^{B29}Tpy-HI with Eu^{3+}, giving longer and less ramified fractals composed of human insulin dimers.

Table S9. Parameters for fractal modelling of SAXS data of HI formulated with Eu^{3+}. The fitted parameters are: Fraction of subunit on fractal form (X_{frac}), fractal dimension (D_f), and fractal correlation length (ξ). Error estimates are given in parentheses.

Metal ion eq.	X_{frac}	D_f	ξ [Å]
1/4 Eu^{3+}	0.71 ($7 \cdot 10^{-3}$)	1.36 ($1 \cdot 10^{-2}$)	323 (15)
1/3 Eu^{3+}	0.72 ($6 \cdot 10^{-3}$)	1.59 ($7 \cdot 10^{-3}$)	603 (27)

4.53 Fractal visualization:

We used FracVAL[22] to produce approximate fractal structures for visualization. FracVAL generates fractals of spherical subunits with the number of spheres, sphere radius, and fractal dimension defined by the user.

In order to generate fractal morphologies relevant for Lys^{B29}Tpy-HI formulated with Eu^{3+}, we used the fractal dimensions (D_f = 2.27, 2.38, 2.66) from the fractal fits to the SAXS data at 1/6, 1/4, and 1/3 Eu^{3+}, respectively, as input to FracVAL. The radius of spherical subunits was given as the average radius (21 Å) of the Lys^{B29}Tpy-HI dimer (Figure S18B). The number of spherical subunits was estimated using the Lys^{B29}Tpy-HI + 1/3 eq. Eu^{3+} sample. Given the large D_f (2.66) for this sample, we approximated a fractal domain as a sphere with radius of $\xi/2$ = 79 Å. This volume can contain 35 spherical subunits of r = 21 Å if randomly packed (i.e. packing efficiency = 64%). This number approximates the minimum number of spheres (39) accepted by FracVAL, which we hence used for building all fractal structures.

Assuming 39 subunits per fractal domain at all Eu^{3+} concentrations enabled visualization of the influence of D_f on fractal morphology, see Figure S13D. The reduction in fractal domain size with increasing D_f qualitatively agrees with the inverse relationship between D_f and ξ (Table S8).

We emphasize that these models are for illustration purposes only, since an infinite variety of fractals can have the same D_f and the models entirely neglect the molecular details of the Lys^{B29}Tpy-HI dimer.

5.0 Spectroscopic studies:

5.1 CD Spectroscopy:

CD was performed on a Jasco J-815 CD spectrometer equipped with a Jasco CDF-426 S/15 controller and a Julabo F12 temperature controller with a path length of 1 mm. Concentration Lys^{B29}Tpy-HI in each sample is 20 µM. CD spectra were collected between 195 and 270 nm, and each spectrum was the average of 5 scans. The buffer spectrum was subtracted before any measurements to eliminate the contribution of buffer (10 mM Tris Buffer, pH 7.5).

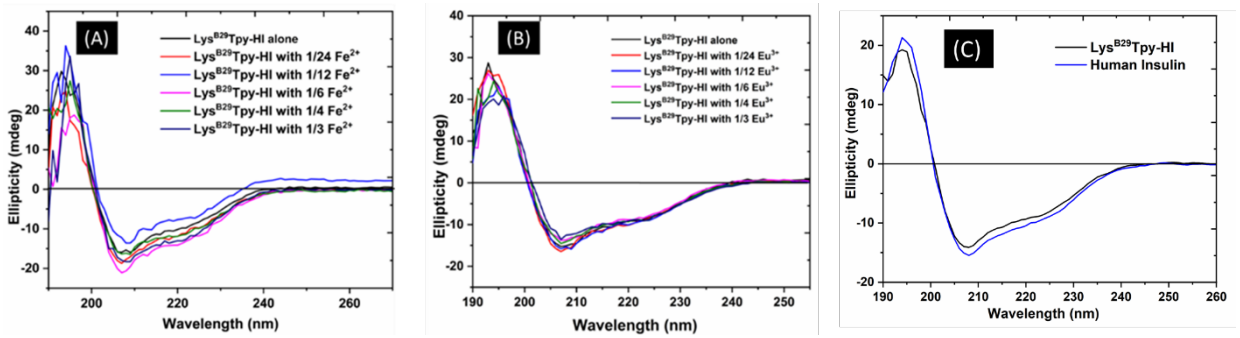

Figure S23: CD spectra of Lys^{B29}Tpy-HI (20 µM) with **(A)** different equivalents of Fe^{2+} **(B)** different equivalents of Eu^{3+} **(C)** Comparison spectra of HI and Lys^{B29}TpyHI at Conc. (15 µM).

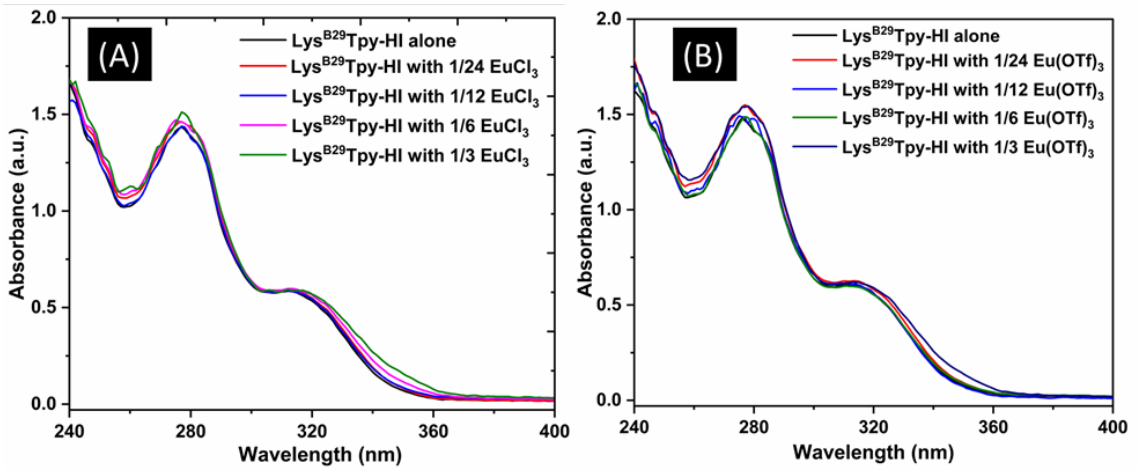

Figure S24: UV Vis spectra of Lys^{B29}Tpy-HI in D_2O **(A)** In presence of $EuCl_3$ **(B)** In presence of $Eu(OTf)_3$

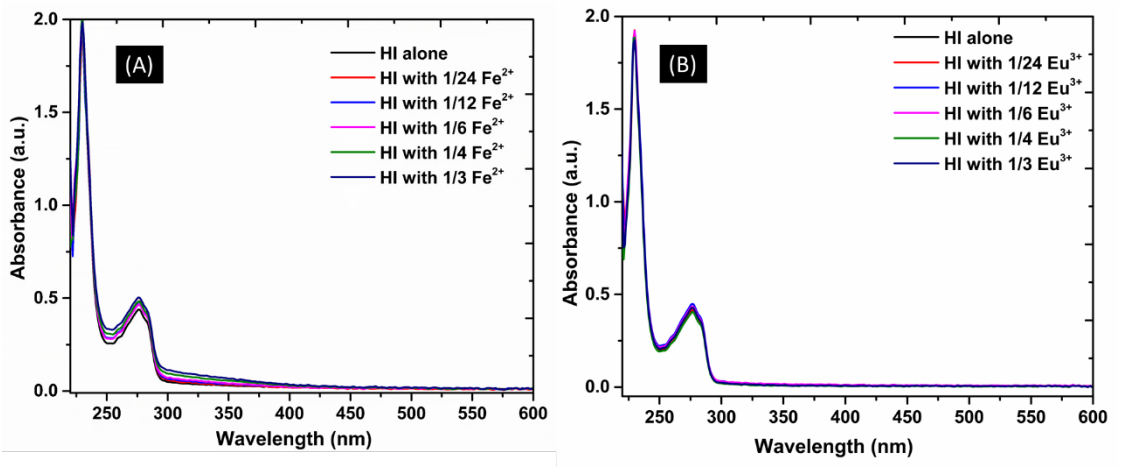

Figure S25: UV Vis spectra of HI in H_2O in presence of **(A)** Fe^{2+} **(B)** Eu^{3+}

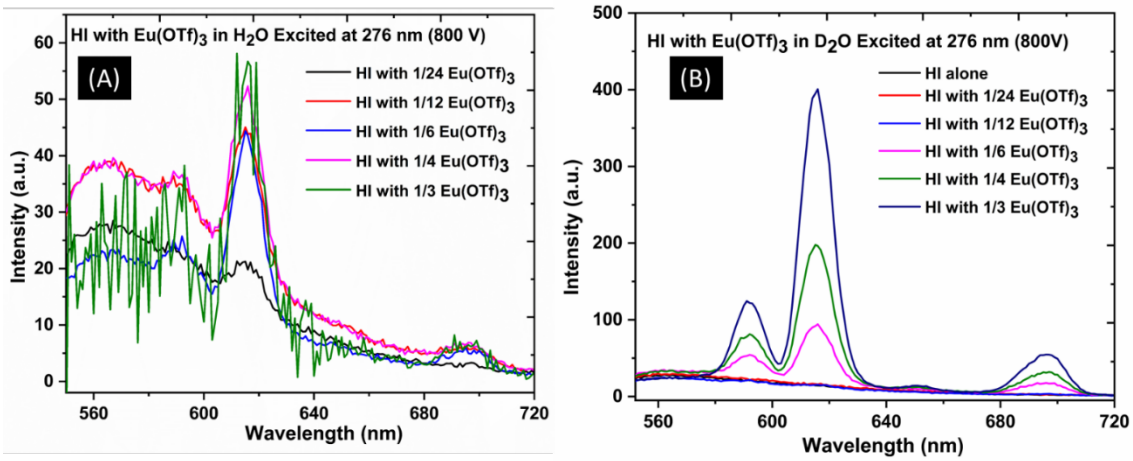

Figure S26: Photoluminescence spectra of HI in presence of Eu^{3+} **(A)** In H_2O **(B)** In D_2O

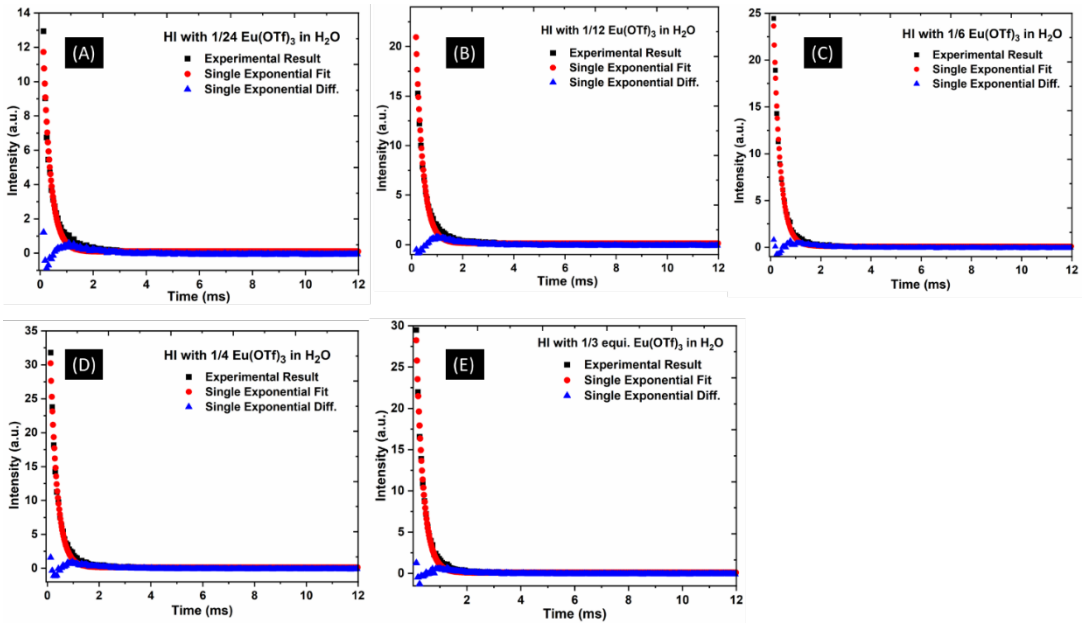

Figure S27: Lifetime spectra of HI with different equivalents of $Eu(OTf)_3$ in H_2O excited at 276 nm

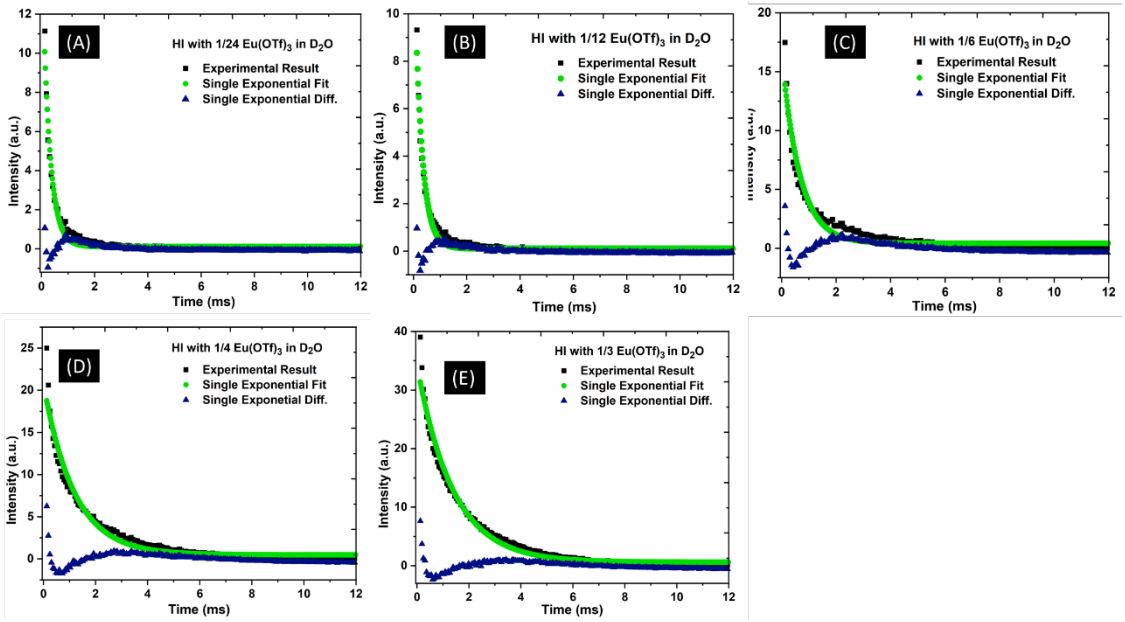

Figure S28: Photoluminescence spectra of HI with different equivalents of $Eu(OTf)_3$ in D_2O excited at 276 nm

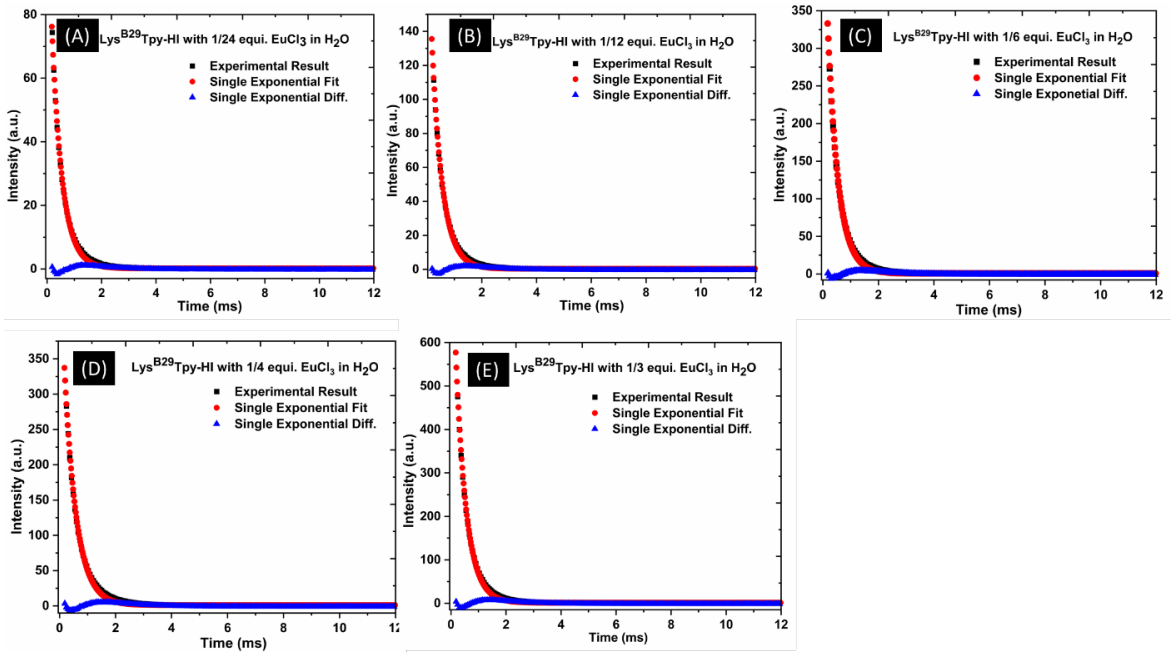

Figure S29: Lifetime spectra of Lys^{B29}Tpy-HI with different equivalents of $EuCl_3$ in H_2O excited at 350 nm

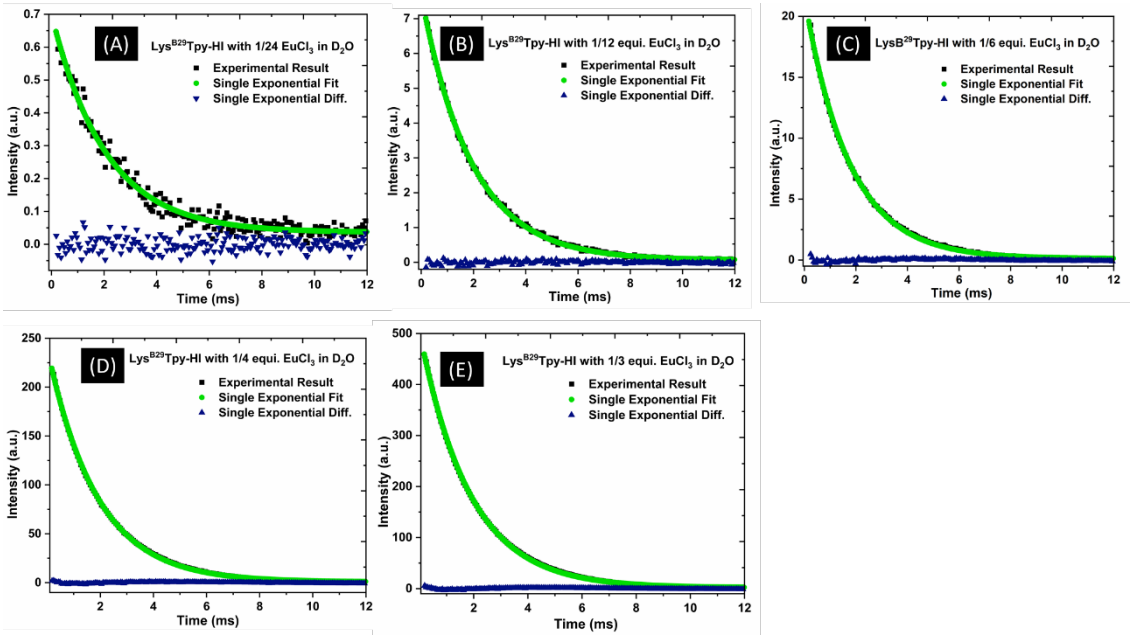

Figure S30: Lifetime spectra of Lys^{B29}Tpy-HI with different equivalents of $EuCl_3$ in D_2O excited at 350 nm

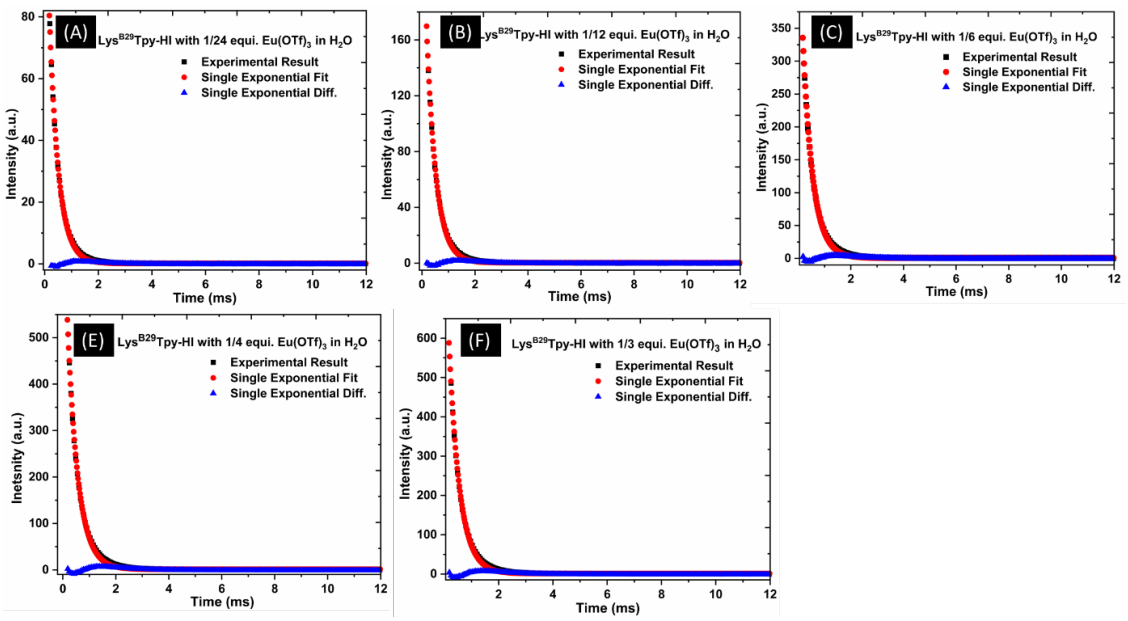

Figure S31: Lifetime spectra of Lys^{B29}Tpy-HI with different equivalents of $Eu(OTf)_3$ in H_2O excited at 350 nm

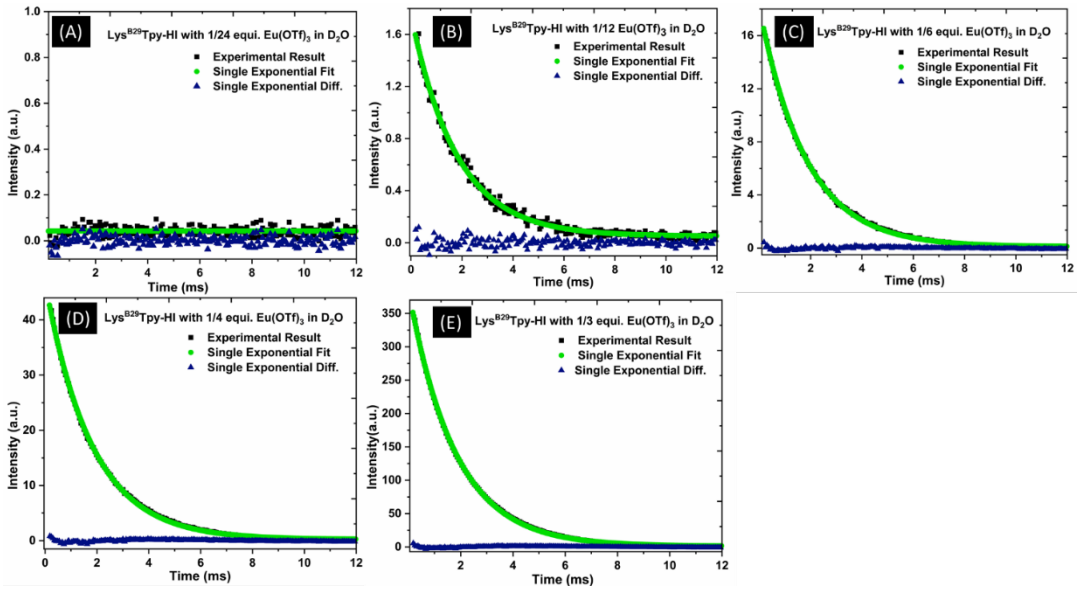

Figure S32: Lifetime spectra of Lys^{B29}Tpy-HI with different equivalents of Eu(OTf)$_3$ in D$_2$O excited at 350 nm.

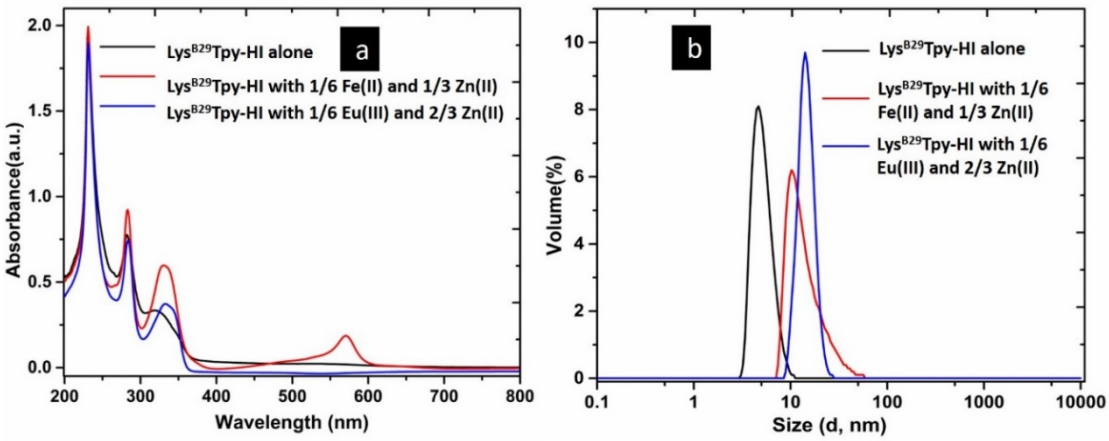

Figure S33: (A) UV-Vis spectra of Lys^{B29}*Tpy*-HI alone and with Fe^{2+} & Zn^{2+} and Eu^{3+} & Zn^{2+} **(B)** DLS spectra of Lys^{B29}*Tpy*-HI with Fe^{2+}/Zn^{2+} and Eu^{3+}/Zn^{2+}.

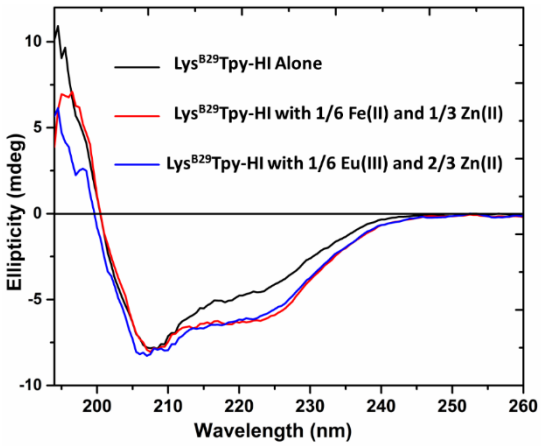

Figure S34: CD spectra of Lys^{B29}*Tpy*-HI with Fe^{2+}, Eu^{3+} in presence of Zn^{2+}

6. X-ray crystallography:

X-ray methods:

200 µL of 600 µM Lys^{B29}Tpy-HI containing 600 µM Fe^{2+}, 200 µM Zn^{2+} and 10 mM Tris pH 7.5 was upconcentrated 3 times and subjected to crystallization screenings in vapour diffusion drops, using a number of commercial screens including the Morpheus screen from Molecular Dimensions, which resulted in a number of crystal hits. Several data sets were tested and collected at cryo-temperatures primarily at the ESRF synchrotron, Grenoble, France. Data were processed with XDS/XSCALE (1) and usually extended to better than 1.7 Å resolution. Molecular replacement was carried out with the CCP4(2) program MOLREP(3), refinement with REFMAC5(4) and inspection of structures with Coot(5).[23-27]

Results

A number of well diffracting data sets were collected throughout the project. Crystals grown in the presence of Fe^{2+} ions were magenta (Figure S35 Left), indicating some incorporation of the metal. All analyzed crystals belonged to the cubic space group $I2_13$ with the typical cell dimensions of a =b =c of around 78 Å. The cell and packing are typical for cubic insulin crystals, which form from dimeric insulin subunit and display a three-fold symmetry axis at the C-terminal of the B chain. The terpy moiety could never be visualized in the electron density, in fact the density is also poor for Lys^{B29}. Since dimeric complexation at a three-fold symmetry axis would leave one terpy moiety unbound or bound to a Fe^{2+} atom coordinating other ligands such as H_2O or Cl^-, both of which are asymmetric scenarios, this is not surprising. Processing without imposing the cubic symmetry (in P1) did not allow visualization of the terpy moiety or the metal.

The lanthanide Eu^{3+} is capable of binding three terpy moieties. Since the Tpy ligand of Lys^{B29}Tpy-HI is found at a three-fold symmetry axis in the crystal structures obtained, we hypothesized that crystal formation in the presence of Eu^{3+} could yield a structure with defined electron density at the ligand site through equivalent and symmetric binding to all three terpy ligands. However, two enantiomers of the $(Lys^{B29}Tpy\text{-}HI)_3Eu^{3+}$ complex exist, which could give rise to disorder at the Eu^{3+} site. In fact, also all crystals grown in the presence of Eu^{3+} belonged to the known cubic from (Figure S35 Right) and did not allow visualization of the Tpy moiety or the metal.

All efforts to obtain non-cubic insulin crystals by altering metal ratio, or using literature crystallization conditions known to promote growth of hexameric insulin[28-30] failed to produce anything but the cubic insulin crystals.

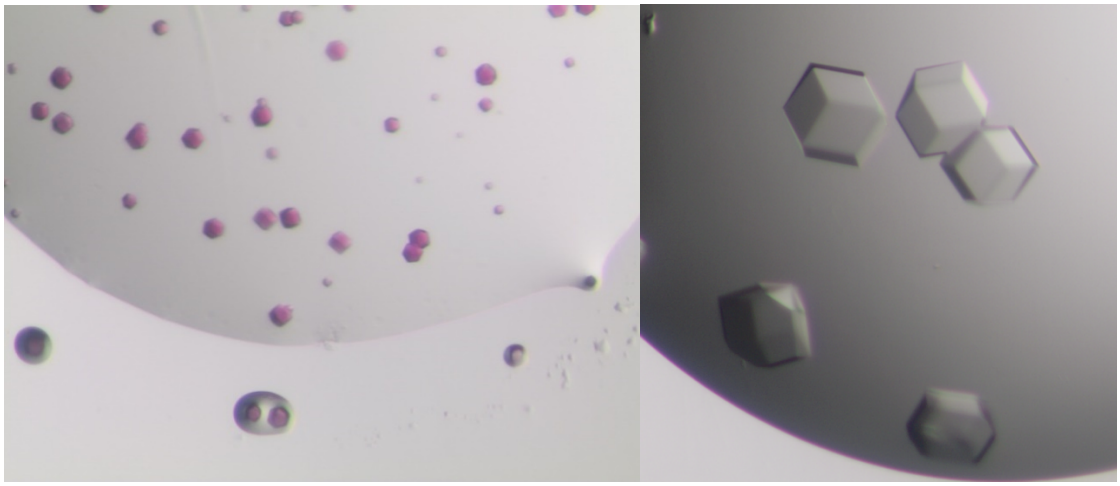

Figure S35: Examples of protein crystals of terpy-HI. **Left:** Magenta cubic crystals formed in the presence of Fe^{2+}. **Right:** Transparent cubic crystals formed in the presence of Eu^{3+}.

7.0 Sample preparation for AFM Studies:

Fresh samples of Lys^{B29}Tpy-HI with 1/6 Fe^{2+} and 1/12 Eu^{3+} were imaged with an atomic force microscope (Cypher, Oxford instruments) operating under the alternating current (AC) mode, with the aid of a cantilever (AC240 from Olympus). The force constant was 2 N/m, while the resonant frequency was around 75 kHz. The images were taken in air at room temperature, with the scan speed of 1−2 lines/s. The data acquisition was done using special AFM control software developed on the Igor pro (7.0) platform. The subsequent data analysis was done with the control software. A portion of 10 µL of samples was deposited onto a freshly cleaved mica surface at room temperature. The sample was uniformly spread using a spin-coater operating at 200−500 rpm (PRS-4000). The sample-coated mica was dried at room temperature in a dust-free space for 60 min followed by AFM imaging.

8.0 *In vitro* cellular signalling study

A monoclonal CHO cell-line overexpressing the human insulin receptor b (hIR-B) was established by transfecting a hIR-B expressing plasmid (HG11081-UT, Sino Biological Inc,) into CHO cells (European Collection of Authenticated Cell Cultures (ECACC)) followed by hygromycin (10687010, Invitrogen) treatment and selection of a clonal cell-line with high hIR-B expression. Cells were maintained in complete media (Ham's F-12 Nutrient Mixture with 10% (v/v) fetal bovine serum (FBS) and 1% penicillin/streptomycin + hygromycin) and seeded (w/o hygromycin) at 25,000 cells per well in a 96-well plate one day prior to the experiment. Cells were starved for 1 h before stimulation in 0.1% (v/v) FBS containing medium, followed by washing and stimulation in DPBS and 0.1% (w/v) BSA. Cells were stimulated for 15 min at 37°C followed by cell lysis and quantification of phosphorylated Akt (Ser473) according to the manufacturer's protocol (Cisbio) (Figure S36).

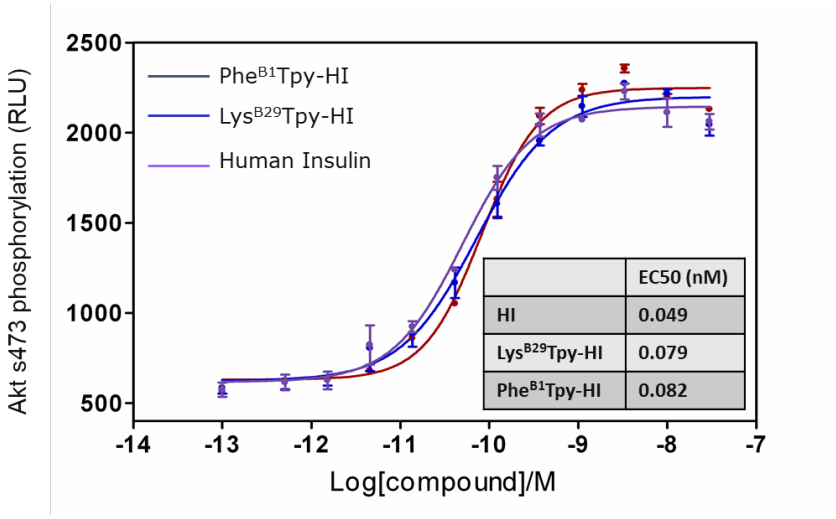

Figure S36: Receptor affinity of human insulin (HI), Lys^{B29}Tpy-HI and Phe^{B1}Tpy-HI.

9. In vivo pharmacokinetic (PK) studies

Male Sprague-Dawley rats (Janvier Labs, Le Genest-Saint-Isle, France) were housed in groups of six per cage, in a reversed light cycle, with standard rodent feed and water for 1 week for acclimatization before the experiment. Prior to the experiment, the rats were fasted on bedding for 12 h during the inactive part of the cycle, with access to water. The animals were further fasted 6 h during the experiments, with access to water. The animals (weighing 260 ± 16 g at the day of the experiment, n = 40) were divided in groups and randomly assigned to receive the different formulations. Each formulation was dosed subcutaneously (SC) and interscapularly, and blood sampling was done over 6 h. The studies were performed under license no. 2016-15-0201-00892 according to Danish law on animal experiments, approved by the Danish Animal Experiments Inspectorate, and all procedures were carried out in compliance with EC Directive 86/609/EEC.

The study was designed with seven groups (n = 4 – 6), where five groups received the insulin analogues (Lys^{B29}Tpy-HI, Lys^{B29}Tpy-HI + Fe^{2+}, Lys^{B29}Tpy-HI + Eu^{3+}, Phe^{B1}Tpy-HI, Phe^{B1}Tpy-HI + Fe^{2+} and Phe^{B1}Tpy-HI + Eu^{3+}) by SC injection with an average volume of 0.26 ± 0.02 mL. Further, one group received the positive control of 1 IU/kg human insulin (HI), and one group received the negative control (Tris buffer). The dose of the analogues was based on calculating the relation between the molecular weight of the analogues and the molecular weight of commercial insulin, and converting into international units (IE), corresponding to a normal dose of commercial insulin. Blood samples (200 µL) were drawn from the tail vein into ethylenediaminetetraacetic acid (EDTA)-coated Microvette® 200 K3E tubes (Sarstedt, Nümbrecht, Germany) at 0, 0.25, 0.5, 0.75, 1, 1.5, 2, 4, and 6 h. Blood glucose concentrations were determined immediately with a Contour® XT meter (Ascensia Diabetes Care, Basel, Switzerland). Blood collected in the Microvette® was centrifuged at 9300 × g for 10 min at 4 °C in a Microcentrifuge 5415 R (Eppendorf, Hamburg, Germany). Plasma was retrieved from the supernatant, and stored at −20 °C, until insulin quantification by enzyme-linked

immunosorbent assay (ELISA) as described by the supplier (ChrystalChem, Elk Grove Village, IL, USA). Euthanasia of the rats was done by CO_2/O_2 gassing.

Data analysis

Data from the *in vivo* PK study is shown as mean ± standard error of the mean (SEM) with n representing biological replicates. Graphs and statistical analysis were performed in GraphPad Prism version 9 (GraphPad software, La Jolla, CA, USA). Statistical significance was determined as $p < 0.05$, using a Student's t-test with or without Welch's correction.

Results

Figure S37A,B,C displays the change in blood glucose in rats recorded over 6h, and Figure S37D,E,F the corresponding insulin plasma concentrations for the six groups receiving the analogues and controls. For Lys^{B29}Tpy-HI, Lys^{B29}Tpy-HI + Fe^{2+} and Lys^{B29}Tpy-HI + Eu^{3+}, the effect on the blood glucose was at its' maximum with a decrease of 56 ± 3% at 66 ± 9 min, 49 ± 5% at 72 ± 9 min, and 61 ± 2% at 54 ± 10 min, respectively (Fig. S37A and Fig. 5A). The blood glucose started rising again at 45 min (Lys^{B29}Tpy-HI,) and 60 min (Lys^{B29}Tpy-HI + Fe^{2+} and Lys^{B29}Tpy-HI + Eu^{3+}) reaching 60 – 70% of the initial blood glucose after 120 min. For Phe^{B1}Tpy-HI, Phe^{B1}Tpy-HI + Fe^{2+} and Phe^{B1}Tpy-HI + Eu^{3+} (Fig. S37B), the decrease in blood glucose was 51 ± 7% at 48 ± 5 min, 62 ± 2% at 66 ± 6 min, and 54 ± 4% at 62 ± 8 min, respectively. The formulation containing Phe^{B1}Tpy-HI + Fe^{2+} resulted in a low blood glucose until 60 min, whereas increasing blood glucose levels were observed after 45 min for the non-complexed Phe^{B1}Tpy-HI and the Phe^{B1}Tpy-HI + Eu^{3+}. After 120 min, the blood glucose had increased to 50% of initial value for Phe^{B1}Tpy-HI + Fe^{2+}, 60% for Phe^{B1}Tpy-HI + Eu^{3+}, and 70% for Phe^{B1}Tpy-HI. The positive control of human insulin (HI) lowered the blood glucose to a moderate level at 71 ± 1% after 36 ± 4 min (Fig. S37C and Fig. 5C). The blood glucose level increased after 60 min, reaching 50% of the initial value at 120 min. The negative control, consisting of tris buffer, displayed a continuous decline in blood glucose over time, and reached its' lowest point at 6 h (23 ± 15 % at 360 min).

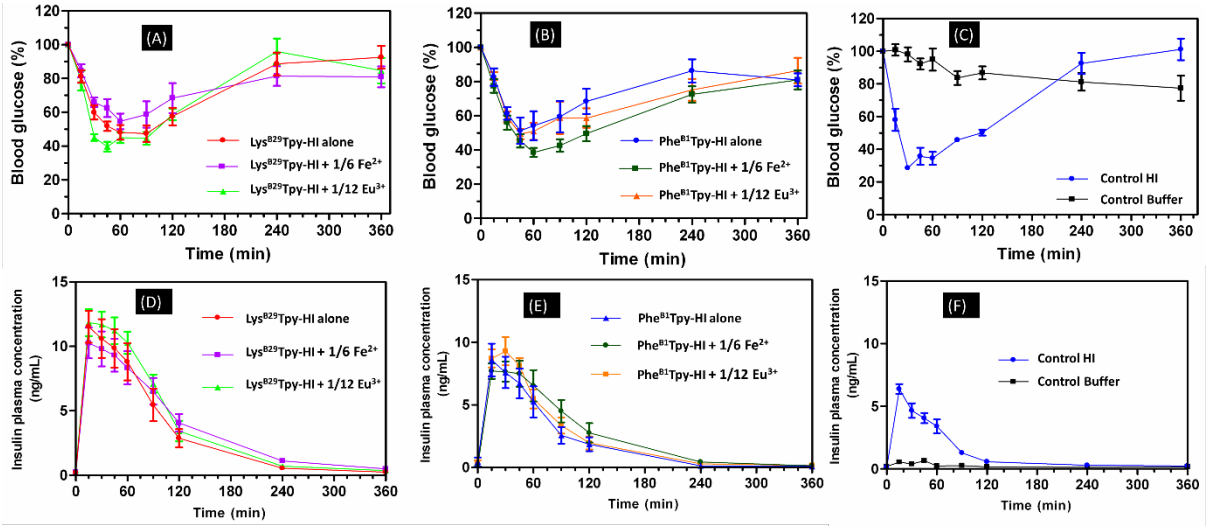

Figure S37 A-C: Change in blood glucose in rats over 6 h after subcutaneous (s.c.) injections of **A:** Lys^{B29}Tpy-HI, Lys^{B29}Tpy-HI + Fe^{2+} and Lys^{B29}Tpy-HI + Eu^{3+}, **B**: Phe^{B1}Tpy-HI, Phe^{B1}Tpy-HI + Fe^{2+} and Phe^{B1}Tpy-HI + Eu^{3+}, and **C:** Human insulin (HI) and buffer. **D-F**: Insulin plasma concentration of **D:** Lys^{B29}Tpy-HI, Lys^{B29}Tpy-HI + Fe^{2+} and Lys^{B29}Tpy-HI + Eu^{3+}, **E:** Phe^{B1}Tpy-HI, Phe^{B1}-Tpy-HI + Fe^{2+} and Phe^{B1}Tpy-HI + Eu^{3+}, and **F:** Human insulin (HI) and buffer. All formulations are dosed in 1 international unit (IU)/kg. Data represents mean ± standard error of the mean (SEM) (n = 4 – 6).

Further, the concentrations of the insulin analogues and the control HI were measured in the plasma. The results are displayed in Fig. S37D – F (and Figure 5B and 5D for Lys^{B29}-Tpy-analogues, HI, and buffer), and the PK parameters are presented in Table S10. The graph displays that the plasma levels of Lys^{B29}Tpy-HI, Lys^{B29}Tpy-HI + Fe^{2+} and Lys^{B29}Tpy-HI + Eu^{3+} are at their highest around 15 min, declining over 360 min, and that all three formulations provide detectable amounts of insulin (ranging from 2-4 ng/mL) at 120 min. For the Phe^{B1}Tpy-HI, Phe^{B1}Tpy-HI + Fe^{2+} and Phe^{B1}Tpy-HI + Eu^{3+}, Phe^{B1}Tpy-HI has a clear peak at 15 min, where Phe^{B1}Tpy-HI + Fe^{2+} seems to flatten out, possibly indicating a peak between the blood sampling times, and Phe^{B1}Tpy-HI + Eu^{3+} peaks at 30 min. At 120 min, the concentrations of the three formulations range from 2-3 ng/mL. The HI control shows a clear peak at 15 min, with a 0.5 ng/mL concentration of insulin in plasma at 120 min, and barely measurable at 240 min.

The PK parameters show a C_{max} that in general is higher for the Lys^{B29}Tpy-HI analogues, compared to the Phe^{B1}Tpy-HI analogues. C_{max} for Lys^{B29}Tpy-HI and Lys^{B29}Tpy-HI + Eu^{3+} are significantly higher than all the other analogue formulations, with 12 ± 3 and 12 ± 2 ng/mL, respectively. All analogue formulations had significantly higher C_{max} than the HI control and the buffer control. T_{max} was around 22-25 min for all formulations, without any significant differences. The area under the curve (AUC) plotted for the plasma concentration versus time over 24 h, reveals a trend of higher AUC_{total} for Lys^{B29}-Tpy-HI analogues, compared to Phe^{B1}Tpy-HI analogues. AUC_{total} of Lys^{B29}Tpy-HI + Fe^{2+} is significantly higher than Phe^{B1}Tpy-HI, Phe^{B1}Tpy-HI + Fe^{2+} and Phe^{B1}Tpy-HI + Eu^{3+}. Further, AUC_{total} of Lys^{B29}Tpy-HI + Eu^{3+} is significantly higher than Phe^{B1}Tpy-HI, Phe^{B1}-Tpy-HI + Fe^{2+} and Phe^{B1}Tpy-HI + Eu^{3+} as well. AUC_{total} of all analogue formulations were significantly different from the two controls (HI and buffer).

Table S10: Pharmacokinetic (PK) parameters of six insulin analogue formulations, along with positive and negative control. Data represents mean ± SEM (n = 5 – 6, n for buffer = 4).			
	C_{max} (ng/mL)	**T_{max} (min)**	**AUC_{Total} (ng × min/mL)**
Lys^{B29}Tpy-HI	12 ± 3	22 ± 13	1353 ± 270
Lys^{B29}Tpy-HI + Fe^{2+}	10 ± 3	24 ± 13	1520 ± 222
Lys^{B29}Tpy-HI + Eu^{3+}	12 ± 2	24 ± 13	1449 ± 153
Phe^{B1}Tpy-HI	9 ± 3	25 ± 12	740 ± 126
Phe^{B1}Tpy-HI + Fe^{2+}	8 ± 2	24 ± 13	928 ± 131
Phe^{B1}Tpy-HI + Eu^{3+}	10 ± 3	24 ± 8	874 ± 109
HI	7 ± 0	18 ± 7	516 ± 38
Buffer	1 ± 0	99 ± 146	143 ± 46

Values marked with letters denote a significant difference ($p < 0.05$).

10. Size exclusion chromatography:

The samples were separated by the size on a fast protein liquid chromatography system (GE ÄKTA purifier 10 system with monitor UV-900 and sample pump P-900). The size exclusion chromatography was carried on a calibrated Superdex 75 10/300 column at room temperature. The injection volume of each sample was 50 µL and used PBS buffer at pH 7.5 as running buffer with a flow of 0.5 mL/min over 1 column volume (CV). The column was equilibrated with 2 CVs (1 CV = 24 mL) of running buffer prior to the injection and the sample was monitored at 280, 330, and 570 nm. The column was calibrated with molecular weight (MW) calibration standards containing Blue Dextran 2000, Conalbumin, Ovalbumin, Carbonic anhydrase, Ribonuclease, and Aprotinin. Molecular weights of each sample were calculated

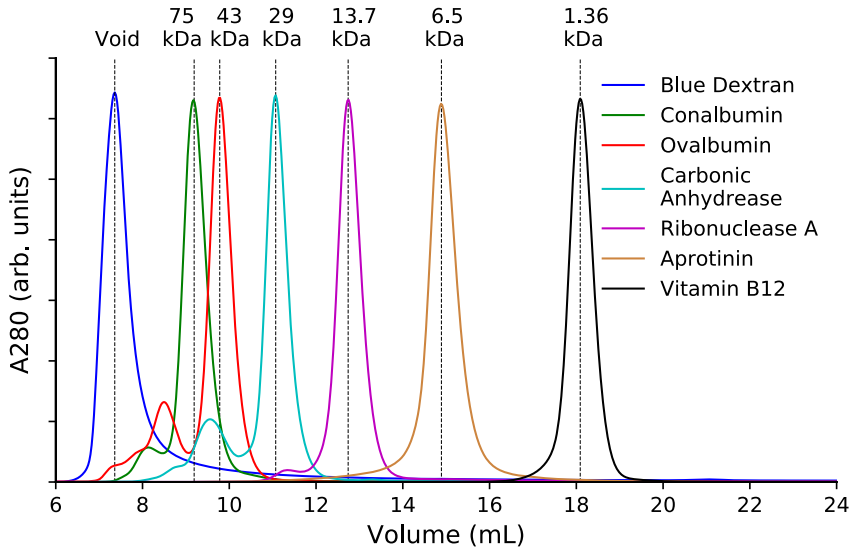

Figure S38: SEC of standard samples were carried out on a Superdex 75 10/300 column applying a flow of 0.5 mL/min PBS buffer at pH 7.5 (room temperature).

by the linear calibration curve of retention volume versus log(MW) of the calibration standard proteins.

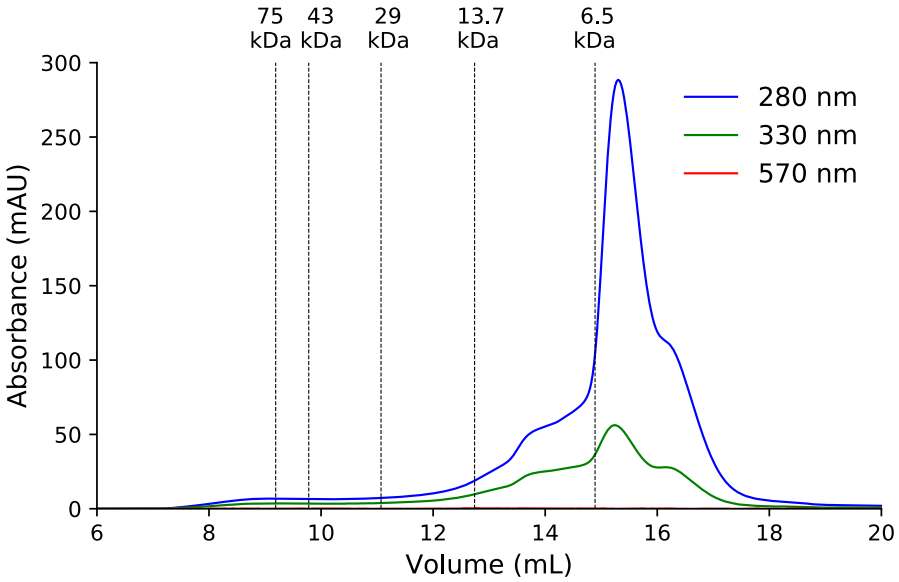

Figure S39: 50 µL injection of 600 µM Lys^{B29}Tpy-HI in 10 mM tris buffer at pH 7.5. The molecular weight of standard proteins is depicted by dotted lines.

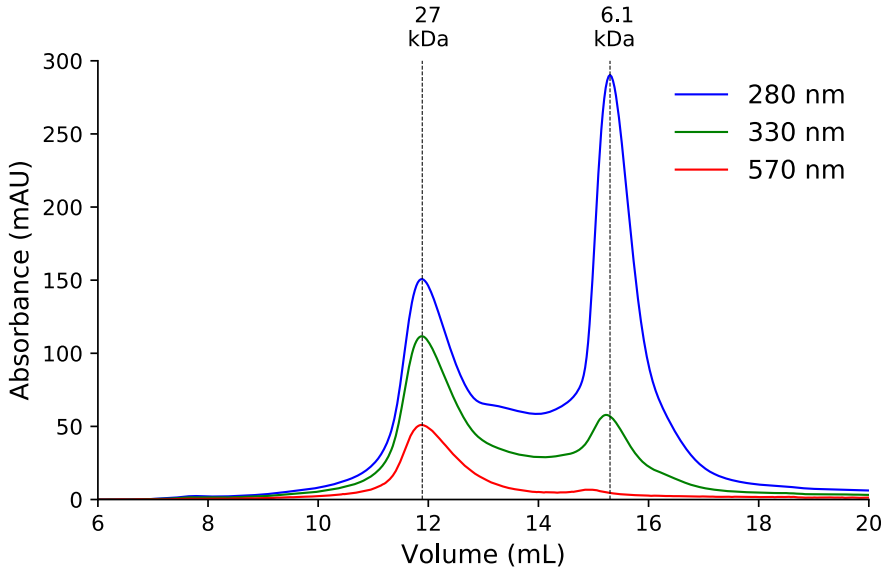

Figure S40: SEC of 600 µM Lys^{B29}Tpy-HI with 1/6 equiv. Fe^{2+} showed the dissociation of tetramer complexes at 11.9 mL (27 kDa). The absorbance at 570 nm at 11.9 mL indicated the presence of Fe^{2+} in the complexes.

As seen in Fig S40 by comparing with data from Fig. S38 the elution peak at 11.9 mL corresponds to the size of an insulin tetramer. The LysB29TpyHI:Fe^{2+} ratio can be roughly assessed using molar absorbance values of ε(280nm) = 2.1583 ·10^4 $M^{-1}cm^{-1}$ for LysB29TpyHI and an approximated ε(570nm) = 1.5 ·10^4 $M^{-1}cm^{-1}$ for the bis(LysB29TpyHI) Fe^{2+} complex. This latter molar absorbance value for 570 nm is not well-defined and the 280 nm value is also subject to a slight increase upon binding of Fe^{2+}. Nevertheless the intensity ratios of the SEC peaks in Fig S40 yields a ratio closely approaching 1:2 for Fe^{2+}:LysB29TpyHI by using A(570nm) = 0.050 for iron and A(280nm) = 0.150 for insulin. The SEC eluted species at 11.9 mL thus in this way

corresponds to a tetramer containing two bis-Tpy units binding one Fe^{2+} each. As the loaded ratio was 1:6 there is internal consistency in the height of the monomer peak eluting at 15.3 mL with A(280 nm) = 290, which corresponds to a 2:4:8 ratio between Fe^{2+}, iron bound, tetrameric LysB29TpyHI and monomeric LysB29TpyHI. On the other hand, the Eu^{3+} bound to LysB29TpyHI is much more labile, as the data in Fig S41 show that the large nanoassemblies formed with the trivalent metal ion largely dissociate during SEC purification, leaving only a minor population of Eu^{3+} bound LysB29TpyHI dimers eluting at 13.4 mL with the remaining LysB29TpyHI eluting as a monomeric species.

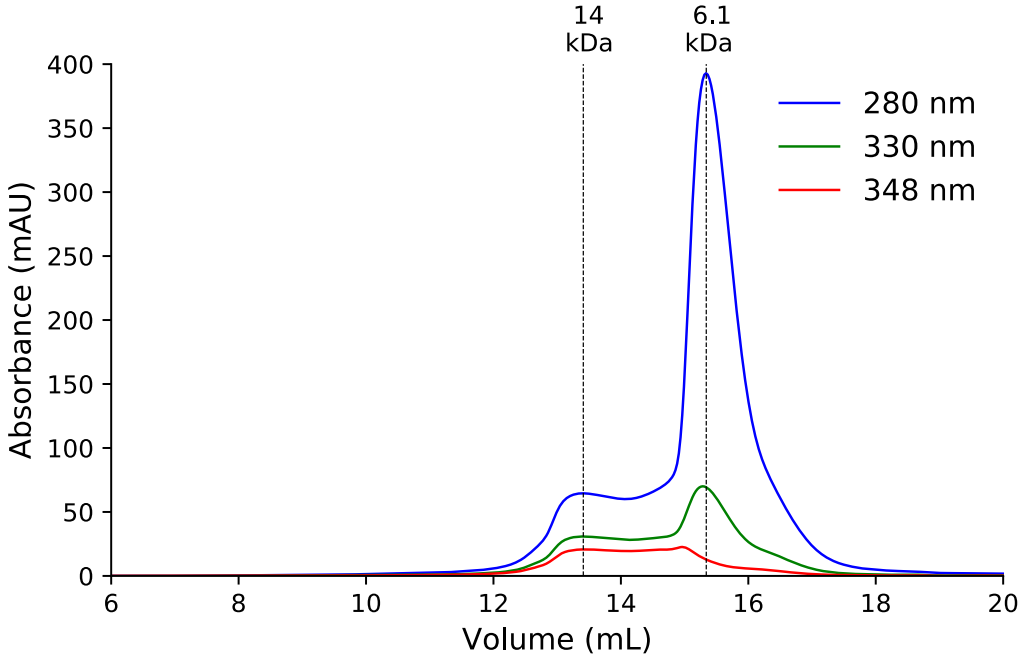

Figure S41: SEC of 600 µM Lys^{B29}Tpy-HI with 1/6 equiv. Eu^{3+} showed two peaks at 13.4 mL (14 kDa) and 15.3 mL (6.1 kDa) indicating dimers and monomers. The remaining intensity in the 348 nm trace at 15.3 mL indicated the presence of Eu^{3+} in the dimers.

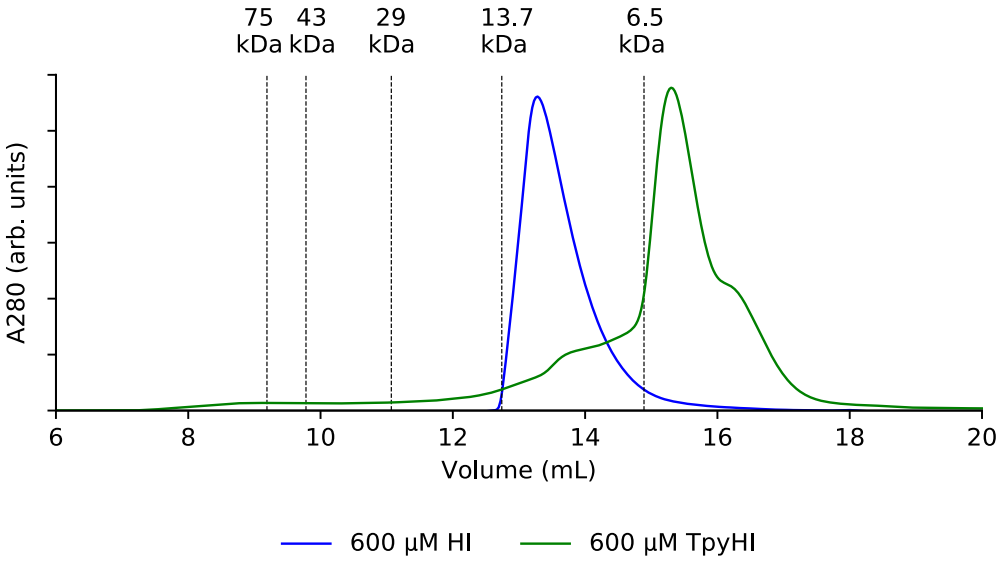

Figure S42: Comparison of SEC spectra of for HI and Lys^{B29}*Tpy*-HI alone

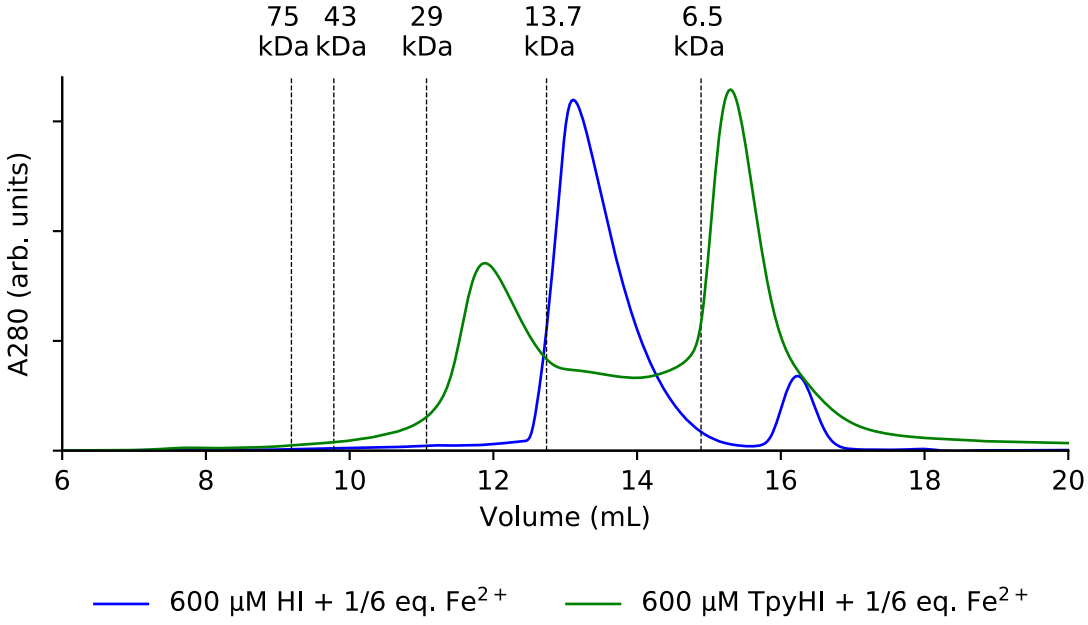

Figure S43: Comparison of SEC spectra of HI and Lys^{B29}*Tpy*-HI with 1/6 Fe^{2+}

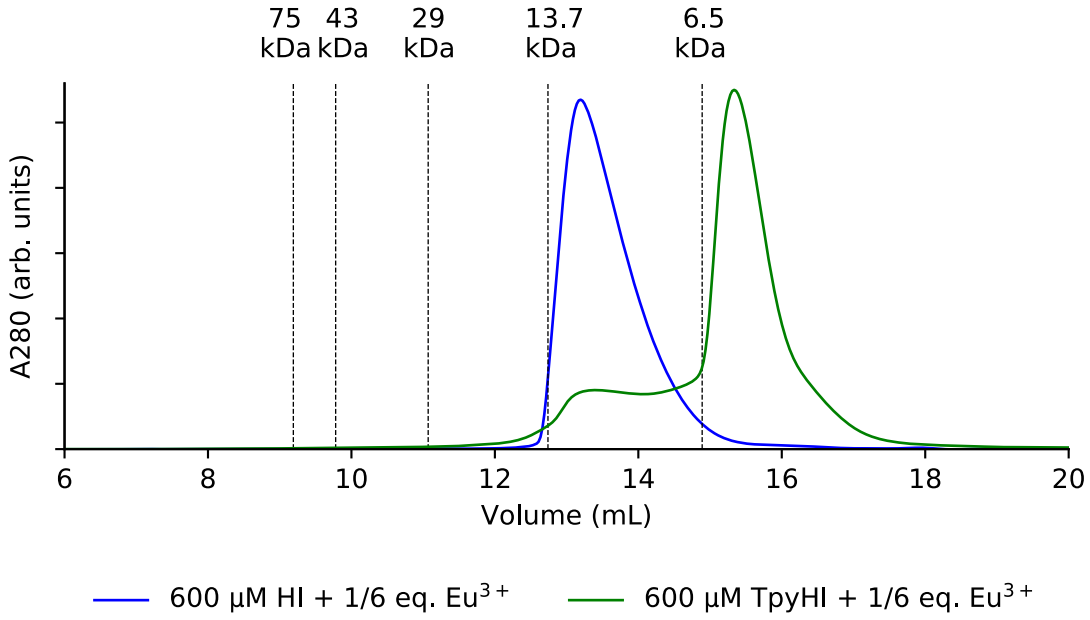

Figure S44: Comparison of SEC spectra of HI and Lys^{B29}Tpy-HI with 1/6 Eu^{3+}

References:

[1] M. Østergaard, N. K. Mishra, K. J. Jensen, *Chem. Eur. J.* **2020**, *26*, 8341-8357.

[2] H. K. Munch, S. T. Heide, N. J. Christensen, T. H-Jensen, P. W. Thulstrup, K. J. Jensen, *Chem. Eur. J.* **2011**, *17*, 7198-7204.

[3] H. K. Munch, J. Nygaard, N. J. Christensen, C. Engelbrekt, M. Ostergaard, T. Porsgaard, T. Høeg-Jensen, J. Zhang, L. Arleth, P. W. Thulstrup, K. J. Jensen, *Angew. Chem. Int. Ed.* **2016**, *55*, 2378-2381

[4] M. V. Petoukhov, D. Franke, A. V. Shkumatov, G. Tria, A. G. Kikhney, M. Gajda, C. Gorba, H. D. T. Mertens, P. V. Konarev, D. I. Svergun, *J. Appl. Crystallogr.* **2012**, *45*, 342-350.

[5] D. Franke, M. V. Petoukhov, P. V. Konarev, A. Panjkovich, A. Tuukkanen, H. D. T. Mertens, A. G. Kikhney, N. R. Hajizadeh, J. M. Franklin, C. M. Jeffries, D. I. Svergun, *J. Appl. Crystallogr.* **2017**, *50*, 1212-1225.

[6] M. C. Pedersen, L. Arleth, K. Mortensen, *J. Appl. Crystallogr.* **2013**, *46*, 1894-1898.

[7] S. Hansen, *J. Appl. Crystallogr.* **2012**, *45*, 566-567.

[8] J. B. Hopkins, R. E. Gillilan, S. Skou, *J. Appl. Crystallogr.* **2017**, *50*, 1545-1553.

[9] (a) D. Orthaber, A. Bergmann, O. Glatter, *J. Appl. Crystallogr.* **2000**, *33*, 218-225; (b) E. Mylonas, D. I. Svergun, *J. Appl. Crystallogr.* **2007**, *40*, s245-s249.

[10] D. Schneidman-Duhovny, M. Hammel, J. A. Tainer, A. Sali, *Nucleic Acids Res.* **2016**, *44*, W424-W429.

[11] J. Teixeira, *J. Appl. Crystallogr.* **1988**, *21*, 781-785.

[12] J. Nygaard, H. K. Munch, P. W. Thulstrup, N. J. Christensen, T. Hoeg-Jensen, K. J. Jensen, L. Arleth, *Langmuir* **2012**, *28*, 12159-12170.

[13] A. H. Larsen, J. S. Pedersen, L. Arleth, *J. Appl. Crystallogr.* **2020**, *53*, 991-1005.

[14] D. Svergun, C. Barberato, M. H. J. Koch, *J. Appl. Crystallogr.* **1995**, *28*, 768-773.

[15] M. Kotlarchyk, S. H. Chen, *J. Chem. Phys.* **1983**, *79*, 2461-2469.

[16] W. Bocian, J. Sitkowski, E. Bednarek, A. Tarnowska, R. Kawęcki, L. Kozerski, *J. Biomol. NMR* **2008**, *40*, 55-64.

[17] Y. Bretonnière, M. Mazzanti, J. Pécaut, M. M. Olmstead, *J. Am. Chem. Soc.* **2002**, *124*, 9012-9013.

[18] K. J. Bowers, D. E. Chow, H. Xu, R. O. Dror, M. P. Eastwood, B. A. Gregersen, J. L. Klepeis, I. Kolossvary, M. A. Moraes, F. D. Sacerdoti, J. K. Salmon, Y. Shan, D. E. Shaw, in *SC '06: Proceedings of the 2006 ACM/IEEE Conference on Supercomputing*, **2006**, pp. 43-43.

[19] E. Harder, W. Damm, J. Maple, C. Wu, M. Reboul, J. Y. Xiang, L. Wang, D. Lupyan, M. K. Dahlgren, J. L. Knight, J. W. Kaus, D. S. Cerutti, G. Krilov, W. L. Jorgensen, R. Abel, R. A. Friesner, *J. Chem. Theory Comput.* **2016**, *12*, 281-296.

[20] W. L. Jorgensen, J. Chandrasekhar, J. D. Madura, R. W. Impey, M. L. Klein, *J. Chem. Phys.* **1983**, *79*, 926-935.

[21] J. L. Whittingham, I. Jonassen, S. Havelund, S. M. Roberts, E. J. Dodson, C. S. Verma, A. J. Wilkinson, G. G. Dodson, *Biochemistry* **2004**, *43*, 5987-5995.

[22] J. Morán, A. Fuentes, F. Liu, J. Yon, *Comput. Phys. Commun.* **2019**, *239*, 225-237.

[23] W. Kabsch, *Acta Crystallogr. Sect. D Biol. Crystallogr.* **2010**, *66*, 125–132.

[24] M. D. Winn, C. C. Ballard, K. D. Cowtan, E. J. Dodson, P. Emsley, P. R. Evans, R. M. Keegan, E. B. Krissinel, A. G. W. Leslie, A. McCoy, S. J. McNicholas, G. N. Murshudov, N. S. Pannu, E. A. Potterton, H. R. Powell, R. J. Read, A. Vagin, K. S. Wilson, *Acta Crystallogr. Sect. D Biol. Crystallogr.* **2011**, *67*, 235–242.

[25] A. Vagin, A. Teplyakov, *J. Appl. Crystallogr.* **1997**, *30*, 1022–1025.

[26] G. N. Murshudov, A. A. Vagin, E. Dodson, *Acta Cryst.* **1997**, *D53*, 240–255.

[27] P. Emsley, K. Cowtan, *Acta Crystallogr. Sect. D - Biol. Crystallogr.* **2004**, *60*, 2126–2132.

[28] R. H. Holyer, C. D. Hubbard, S. F. A. Kettle, R. G. Wilkins, *Inorg. Chem.* **1966**, *5*, 622–625

[29] J. L. Whittingham, I. b. Jonassen, S. Havelund, S. M. Roberts, E. J. Dodson, C. S. Verma, A. J. Wilkinson, G. G. Dodson, *Biochemistry* **2004**, *43*, 5987–5995.

[30] J. L. Whittingham, S. Havelund, I. Jonassen, *Biochemistry* **1997**, *36*, 2826–2831